

# A continuous boostlet transform for acoustic waves in space–time

Elias Zea<sup>\*,1</sup>Marco Laudato<sup>2</sup>Joakim Andén<sup>3</sup>

<sup>1</sup>KTH Royal Institute of Technology, Department of Engineering Mechanics, The Marcus Wallenberg Laboratory for Sound and Vibration Research, Teknikringen 8, SE-114 28 Stockholm, Sweden

<sup>2</sup>KTH Royal Institute of Technology, Department of Engineering Mechanics, FLOW Centre, Osquars Backe 18, SE-114 28 Stockholm, Sweden

<sup>3</sup>KTH Royal Institute of Technology, Department of Mathematics, Division of Probability, Mathematical Physics and Statistics, Lindstedtvägen 25, SE-114 28 Stockholm, Sweden

March 15, 2024

## Abstract

Sparse representation systems that encode the signal architecture have had an exceptional impact on sampling and compression paradigms. Remarkable examples are multi-scale directional systems, which, similar to our vision system, encode the underlying architecture of natural images with sparse features. Inspired by this philosophy, the present study introduces a representation system for acoustic waves in 2D space–time, referred to as the *boostlet transform*, which encodes sparse features of natural acoustic fields with the Poincaré group and isotropic dilations. Continuous boostlets,  $\psi_{a,\theta,\tau}(\varsigma) = a^{-1}\psi(D_a^{-1}B_\theta^{-1}(\varsigma - \tau)) \in L^2(\mathbb{R}^2)$ , are spatiotemporal functions parametrized with dilations  $a > 0$ , Lorentz boosts  $\theta \in \mathbb{R}$ , and translations  $\tau \in \mathbb{R}^2$  in space–time. The admissibility condition requires that boostlets are supported away from the acoustic radiation cone, i.e., have phase velocities other than the speed of sound, resulting in a peculiar scaling function. The continuous boostlet transform is an isometry for  $L^2(\mathbb{R}^2)$ , and a sparsity analysis with experimentally measured fields indicates that boostlet coefficients decay faster than wavelets, curvelets, wave atoms, and shearlets. The uncertainty principles and minimizers associated with the boostlet transform are derived and interpreted physically.

## 1 Introduction

Wave equations are mathematical structures central in many fields of physics and engineering, with applications ranging from medical imaging to acoustics, seismic exploration, electromagnetism, and gravitational wave detection. In acoustics, canonical

---

\*Corresponding author: [zea@kth.se](mailto:zea@kth.se).

solutions to the wave equation are well-known in various geometries [1], typically described in planar, cylindrical, and spherical coordinates. From Fourier’s uncertainty principle, planar wave solutions are fully localized in the wavenumber-frequency domain and non-localized in space–time. As a consequence, modeling localized phenomena in space–time—such as wave scattering of an object with a size comparable to the wavelength—is challenging and computationally expensive. A large number of expansion coefficients are needed to model the spatiotemporal wave decay in the near-field. Another challenging aspect of acoustic scattering from a finite object is the transition of the wave from being localized in space–time in the vicinity of the object, with broadband Fourier spectrum, to being spatially extended far away from the object, with band-limited Fourier spectrum. As a consequence of the Sommerfeld radiation boundary condition [2], the compact wave expands spherically outwards and turns into a transient planar wave—becoming a localized ridge in the Fourier domain. How these dynamics are captured by a representation system is key for analyzing and processing acoustic fields in space–time.

The analysis and processing of acoustic fields has seen numerous developments since the first computer simulations in the 1960s [3, 4], when applications of geometrical-acoustics methods, e.g., ray tracing [5], quickly became popular. Some years later, the image source method was developed as an analytical tool to predict acoustical reflections in complex room geometries [6]. In the 1980s, Williams and collaborators made monumental advancements in sound source quantification by introducing acoustic holography [7], an industrial breakthrough for contactless characterization of vibroacoustic sources. By the end of the 1990s, Berkhout *et al.* studied the analysis [8] and extrapolation [9] of acoustic fields inside rooms in great detail by using analogies from seismic exploration. Numerical approaches such as finite elements [10], finite-difference-time-domain methods [11], spectral element methods [12], and discontinuous Galerkin methods [13] have since been used extensively to approximate the solution by discretizing the computational domain. With the emergence of compressed sensing in the mid-2000s [14], numerous studies have investigated the sparse reconstruction of acoustic fields with monopole sources [15, 16], plane waves [17], curvelets [18], and shearlets [19]. Finally, data-driven methods, such as physics-informed neural networks [20, 21, 22, 23, 24], deep prior approaches [25, 26, 27], generative models [28, 29, 30, 31], and neural operators [32, 33, 34, 35], have recently achieved impressive results due to their ability to more closely adapt to the structure (spatial or temporal) of the acoustic fields.

## 1.1 Sparse representation machinery

Sparse representations have had impactful applications in imaging sciences, such as compressed sensing, super-resolution, multi-scale analysis, and feature extraction for model-based and machine-learning frameworks. Indeed, sampling and reconstructing acoustic fields in space–time is challenging because many data points are required to avoid aliasing. For example, in the human audible range (20 Hz to 20 kHz), about 1.6 million microphone positions are necessary to reconstruct the pressure field over a cubic meter of air. Thus, overcoming sampling limitations has a profound impact on technologies based on the wave equation, such as seismic exploration, medical ultrasound, and vibroacoustic imaging, to mention a few.

Decades of efforts in applied harmonic analysis have led to remarkable representation systems. In 1946, Gabor presented a theory for time–frequency analysis [36] by applying Heisenberg’s uncertainty principle and establishing an analogy between sound and quanta. Gabor envisioned that a family of parametrized *atoms* could detect transient components more effectively than Fourier bases. Gabor’s ideas later triggered the development of the wavelet transform in the 1970s, coined initially as the cochlear transform by Zweig [37], and later formalized in various ways by Grossmann, Morlet, Debauchies, and Meyer in the 1980s-1990s [38, 39, 40]. An interesting property of Gabor wavelets is their optimal uncertainty in time and frequency domains simultaneously. Wavelets sit at the core of JPEG2000 compression and offer optimally sparse representations of point singularities in high-dimensional spaces.

The beauty of wavelets lies in their transcendental application in many fields of science and technology. Their limitation, however, is the representation of extended singularities, because of which various anisotropic transforms were constructed in the late 1990s / early 2000s, e.g., ridgelets to represent ridge functions [41], and curvelets [42], shearlets [43], and contourlets [44] to represent curved singularities. Similar variants have been later proposed, such as hyperbolic shearlets [45], alpha molecules [46] and bendlets [47]. These representation systems have been applied successfully to image denoising [48, 49], edge detection [50, 51], and inpainting [52, 53]. Research in microlocal analysis shows that curvelets and shearlets resolve the wavefront set [54, 55]. In the context of acoustics, curvelets [56] and wave atoms [57] have been shown to provide optimally sparse representations of the wave propagator in free space. In this sense, they are functions defined on a so-called space–time foliation, e.g., wave fields evolving from one instant to another with Hamiltonian flows. Demanet and Ying [57] have shown that optimally sparse representations of Fourier integral operators and Green’s function of the wave equation are achieved with anisotropic essential support  $\sim 2^{-aj} \times 2^{-j/2}$ , where  $a \in [1/2, 1]$ . Despite the remarkable progress, literature is scarce on representations in full space–time [58, 59, 60, 61].

## 1.2 Multi-scale directional analysis in acoustic scattering and beyond

Modeling localized wave phenomena in the near-field, for example, the scattered wave highlighted in Fig. 1(b), is challenging when the size of the scattering object is comparable to the acoustic wavelength  $\lambda$ . From the viewpoint of representation sparsity of stationary plane waves, many coefficients must interfere (constructively and destructively) to replicate the wave decay in space–time—especially in the vicinity of the object. Acoustic scattering problems are typically boundary value problems where a sound source ensonifies some finite or infinite body, i.e. causes the latter to scatter the sound wave. The classical approach is to view the total sound field as a sum of the ensonifying sound wave in a completely free field,  $p_{\text{ff}}(\mathbf{r}, t)$ , and a scattered sound wave,  $p_{\text{sc}}(\mathbf{r}, t)$ , which is also assumed to radiate in free space,

$$p(\mathbf{r}, t) = p_{\text{ff}}(\mathbf{r}, t) + p_{\text{sc}}(\mathbf{r}, t),$$

where  $\mathbf{r} = (x, y, z) \in \mathbb{R}^3$  and  $t \in \mathbb{R}$  are the coordinates of 4D space–time. The sum of these two sound field components must fulfill the specified boundary condition in the free space (that is, a non-reflective boundary condition) at the location of the

scattering body’s surface. An orthogonal set of known mode functions (parameterized solutions) exists for a few geometries, such as a sphere, a cylinder, etc. [62]. For these geometries, the boundary condition can be fulfilled mode by mode, and the mode amplitudes for  $p_{sc}(\mathbf{r}, t)$  can be derived. Numerical methods based on the Kirchhoff–Helmholtz integral equation can also predict  $p_{sc}(\mathbf{r}, t)$ . The free-field function  $p_{ff}(\mathbf{r}, t)$  is smooth since it is a propagating sound wave. Therefore,  $p_{sc}(\mathbf{r}, t)$  must also be a smooth function. Nonetheless, corners and edges of the scattering body may cause significant gradients in the pressure fields.

Taking scattering as a challenging applied problem, this study introduces a sparse representation system for localized waves in space–time and wavenumber–frequency domains, preliminarily investigated by Zea and Laudato in [60]. Experimental evidence from data in that study is shown in Fig. 1. In particular, a scattered wave is shown in the zoomed-in box of Fig. 1(b), which has a space–time decay due to the finiteness of the array in Fig. 1(a). Specifically, we see a wave that is attenuated closer to the left end of the array but which is amplified closer to the center. Additionally, the Fourier spectrum in Fig. 1(c) exhibits hyperbolae localized inside a phase velocity cone. These hyperbolae lie in the co-direction of the waves in space–time and correspond to their phase velocities. Here, we mention acoustic scattering as an application for boostlets, and other applications (see above) may further convince the reader of the potential impact. We envision opportunities that benefit technologies based on the wave equation and potentially other partial differential equations.

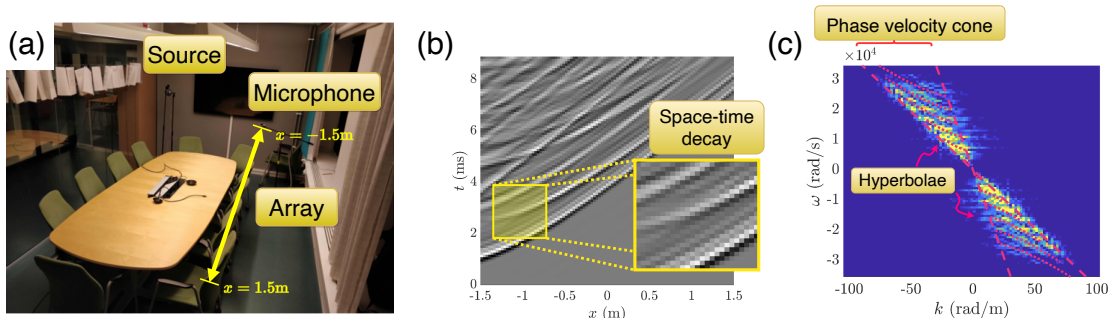


Figure 1: Illustration of a room-acoustical measurement in 2D space–time. (a) Experimental setup with a sound source emitting a frequency sweep between 100 Hz and 4.5 kHz and a free-field microphone recording the sound pressure. (b) Sound pressure field measured for approximately 8.9 ms on a line of 100 microphone positions spanning 3 m. Zoom-in shows a wave decaying in space–time, entailing a scattered wave. (c) Fourier spectrum of (b). The spectrum shows several hyperbolae localized in a phase velocity cone (dashed lines shown for illustration purposes).

### 1.3 Contribution of the work

Previous applications of multi-scale directional transforms to interpolate wavefronts in space–time have proved empirically successful [18, 19]. As mentioned above, these transforms were rightfully designed for image processing, that is, for extended singularities in real space, but not explicitly for waves in full space–time. The central distinction with the boostlet transform is that it considers a unified treatment of

space–time for wave propagation problems; specifically, boostlets encode the physical attributes of a localized wave in a manner equivariant to boosts (or hyperbolic rotations), dilations, and translations in space–time. We find the application of geometric tools from special relativity to sparsely represent waves genuinely fascinating and by no means evident. To the best of our knowledge, the application of such special relativity ideas to represent acoustic waves is new.

The main contributions of this work are summarized in what follows:

- (i) We apply the principle of analogy from sparsely coding natural images [63, 64] to sparsely coding acoustic waves in space–time. Previous theoretical and experimental results [60] indicate that natural acoustic fields in 2D space–time can be sparsely encoded into band-limited wave shapes that are neither planar nor spherical. As Fig. 1(c) suggests, anti-symmetric hyperbolae localized in phase velocity cones characterize these shapes. In this work, we will see that this particular structure can be encoded using a certain group structure (that of the Poincaré group).
- (ii) We introduce the *continuous boostlet transform*, which decomposes acoustic waves into a collection of band-limited functions on  $L^2(\mathbb{R}^2)$ , referred to as *boostlets*, parametrized with the Poincaré group (Lorentz boosts and translations), and isotropic dilations in 2D space–time. The physical meaning of the admissibility condition of the transform and its peculiar scaling function are discussed. When applied to acoustic fields measured experimentally, boostlets exhibit similarities with scattered waves due to their spatiotemporal decay and appear to have a faster coefficient decay compared to benchmark systems such as wavelets, shearlets, and wave atoms.
- (iii) We derive the uncertainty principles associated with the continuous boostlet transform and the corresponding minimizers for the transform parameter pairs. We discuss their physical interpretation and compare them with the uncertainty principles of 2D wavelets [65] and 2D shearlets [66]. The infinitesimal generators of the dilation and boost operators commute, indicating the existence of a continuum of wave shapes with various Fourier support sizes that are all optimally concentrated with respect to dilation and boosting, including the canonical cases of planar and spherical waves.

## 2 Background

Although solutions of the wave equations have a wide frequency range, this study focuses on the acoustic regime between infrasound and ultrasound. Our ambition is that the methodology can be extended to other types of waves and propagation media. This section presents the relevant background on canonical solutions to time-harmonic wave equations, Fourier acoustics theory, and encoding dispersion relations with a group structure.

## 2.1 Wave equation preliminaries

The linearized wave equation in a homogeneous medium with constant sound speed, in the absence of flow, is a second-order hyperbolic partial differential equation (PDE) of the form

$$\square p(\mathbf{r}, t) := \left( \nabla^2 - \frac{1}{c_0^2} \frac{\partial^2}{\partial t^2} \right) p(\mathbf{r}, t) = 0, \quad (1)$$

where  $\square$  is known as the d'Alembert operator,  $p(\mathbf{r}, t) \in \mathbb{R}$  is the acoustic pressure at the position  $\mathbf{r}$  and time  $t$ ,  $c_0 \in \mathbb{R}^+$  is the sound speed of the medium (e.g., air at room temperature), and  $\nabla^2$  is the Laplacian operator, defined here in Cartesian coordinates as

$$\nabla^2 = \frac{\partial^2}{\partial x^2} + \frac{\partial^2}{\partial y^2} + \frac{\partial^2}{\partial z^2}.$$

A classical approach to solving the wave equation is to separate the space and time variables and compute the stationary wave solutions by fixing the angular frequency  $\omega = \omega_0 \in \mathbb{R}^+$ , giving

$$p(\mathbf{r}, t) = \hat{p}(\mathbf{r}; \omega_0) e^{-i\omega_0 t}, \quad (2)$$

where  $i$  is the imaginary unit. The separation of variables turns the hyperbolic PDE in Eq. (1) into the elliptic PDE

$$\nabla^2 \hat{p}(\mathbf{r}; \omega_0) + k^2 \hat{p}(\mathbf{r}; \omega_0) = 0, \quad (3)$$

commonly known as the Helmholtz equation in acoustics and electromagnetism. Here, the acoustic wavenumber is  $k_0 = \omega_0/c_0$ ; i.e., acoustic waves are linearly dispersive. A common solution in Cartesian coordinates for Eq. (3) is a plane wave solution of the form

$$\hat{p}(\mathbf{r}; \omega_0) = P(\omega_0) e^{i(\mathbf{r} \cdot \hat{\mathbf{k}})}, \quad (4)$$

where  $P(\omega_0) \in \mathbb{C}$  is the amplitude of the wave at frequency  $\omega_0$ ,  $(\cdot)$  denotes the scalar product, and  $\hat{\mathbf{k}} = (\hat{k}_x, \hat{k}_y, \hat{k}_z)$  is the wavenumber vector with components defined as:

$$\begin{aligned} \hat{k}_x &= k_0 \cos \alpha \sin \beta, \\ \hat{k}_y &= k_0 \sin \alpha \cos \beta, \\ \hat{k}_z &= k_0 \cos \beta, \end{aligned} \quad (5)$$

where  $(\alpha, \beta)$  are the azimuth and elevation angles, respectively, along which the wave propagates.

The spatial Fourier transform of Eq. (4) gives the following Dirac delta located at  $(\hat{k}_x, \hat{k}_y, \hat{k}_z)$  [67]

$$\hat{p}(\mathbf{k}; \omega_0) = \int_{\mathbb{R}^3} P(\omega_0) e^{i(\mathbf{r} \cdot \hat{\mathbf{k}})} e^{-i(\mathbf{r} \cdot \mathbf{k})} d\mathbf{r} = P(\omega_0) \delta(k_x - \hat{k}_x, k_y - \hat{k}_y, k_z - \hat{k}_z),$$

which gives a fully localized representation in Fourier space and a non-localized (global) representation in real space. Similar results exist for cylindrical and spherical waves [67].

Experimental evidence [17] suggests that plane wave expansions can sparsely represent stationary acoustic fields in rooms at low frequencies (i.e., the modal region). In this frequency region, it is known that the acoustic field in the room is composed of a few modes, which can be represented by a few plane waves. Similar reports have indicated that monopole sources provide sparse representations of compact vibroacoustic sources [68, 69], which are fully localized in real space and broadband in the wavenumber domain.

## 2.2 Acoustic radiation in Fourier space

A solution of the linearized wave equation of the form described in Eq. 4 explicitly depends on the wavenumber vector  $\mathbf{k}$  and frequency  $\omega$ . The relation between these two quantities is called the dispersion relation, and for non-dispersive media (e.g., air) reads  $\omega^2 = c_0^2 |\mathbf{k}|^2$ . Plane waves propagate to the far field or decay in the near field (also known as evanescent waves). Consider without loss of generality that a plane wave is propagating or decaying along the  $z$ -direction. Then, propagating waves are smooth periodic functions defined across the whole of space-time and have acoustic wavelengths  $\lambda \geq 2\pi/k_0$ . And evanescent waves are smooth functions that decay exponentially away with  $z$  and have wavelengths  $\lambda < 2\pi/k_0$ . While a propagating wave has a real wavenumber along the  $z$ -direction

$$k_z = \sqrt{k_0^2 - k_x^2 - k_y^2},$$

an evanescent wave has an imaginary wavenumber in that direction

$$k_z = ik'_z = i\sqrt{k_x^2 + k_y^2 - k_0^2}.$$

Substituting the above into (4) gives a propagating plane wave

$$\hat{p}(\mathbf{r}, \omega_0) = P(\omega_0) e^{i(k_x x + k_y y + k_z z)}$$

and an evanescent plane wave

$$\hat{p}(\mathbf{r}, \omega_0) = P(\omega_0) e^{i(k_x x + k_y y)} e^{-k'_z z},$$

respectively.

For all values of  $(k_x, k_y) \in \mathbb{R}^2$  and a specific frequency  $\omega_0$ , propagating and evanescent waves are thus divided by the so-called radiation circle [67]. As illustrated in Fig. 2, the extrusion of the radiation circle as the frequency  $\omega \in \mathbb{R}$  varies results in the radiation cone. The presence of this cone suggests that a natural decomposition of the wavefield must preserve this cone.

## 2.3 Trace waves and phase velocities

While waves of the form in Eq. (4) propagate in three dimensions, we will consider one-dimensional measurements of these wavefields (such as those obtained using a linear microphone array) in this work. The result is a projection of the wavefield along a single spatial coordinate, which induces a one-dimensional wavefield along that coordinate.

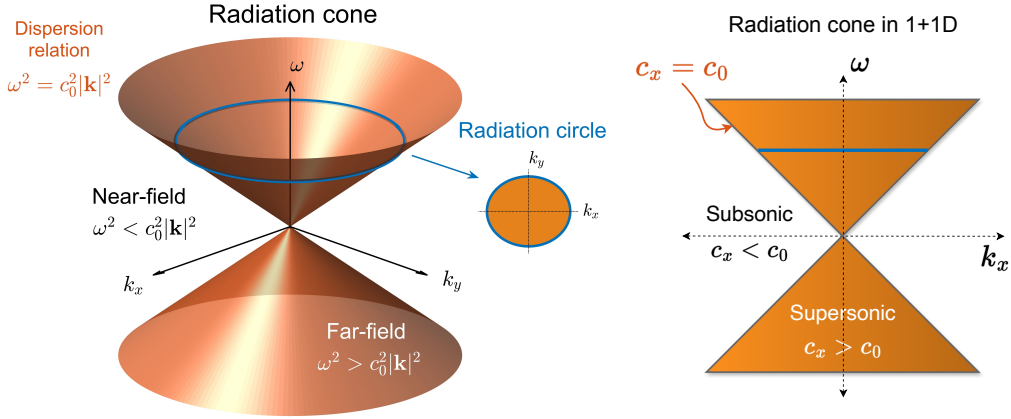


Figure 2: Left: The radiation cone divides acoustic waves into far-field and near-field waves. The radiation circle follows when considering stationary wave solutions, i.e., the Helmholtz equation (3). Right: Projection of the radiation cone in 1+1D, showing the cone regions with supersonic (far-field) and subsonic (near-field) trace waves, i.e., phase velocities greater and smaller than  $c_0$ , respectively. The cone boundary corresponds to a phase velocity equal to  $c_0$ . Cones arise naturally in special relativity due to the principle of causality: a particle inside the cone remains inside the cone. Using the acoustics analogy, a far-field wave inside the radiation cone remains a far-field wave.

From Fourier acoustics theory [67], it is known that the projection of such an acoustic wave along one spatial coordinate, say  $x$ , will result in a so-called *trace wave*

$$p(x, t) = \hat{p}e^{i(k_x x - \omega_0 t)}$$

with amplitude  $\hat{p} \in \mathbb{C}$ , which propagates with a phase velocity  $c_x = \omega_0/k_x$  and has an associated trace wavelength  $\lambda_x = 2\pi/k_x$  and trace wavenumber  $k_x$  along the  $x$ -axis. In the remainder of this paper, we shall denote the trace wavenumber along the  $x$ -axis simply with  $k$ .

Let us consider, without loss of generality, a propagating wave with azimuth angle  $\alpha = 0$  and some elevation angle  $\beta$  with respect to the normal of the  $x$ -axis. Then, using (5), the trace wavenumber  $k = k_0 \sin \beta$ , and the phase velocity along the  $x$ -axis reads  $c_x = c_0/\sin \beta$ . On the one hand, for instance, a propagating wave with  $\beta = \pi/2$  is recorded at a line of receivers on the  $x$ -axis with a phase velocity  $c_x = c_0$ . Similarly, if  $\beta = 0$ , the propagating wave has infinite phase velocity. On the other hand, an evanescent wave has an imaginary  $\beta$ , which results in a phase velocity always smaller than the sound speed  $c_0$  and an exponential decay along the normal of the  $x$ -axis. In other words, as illustrated on the right of Fig. 2, propagating waves are inside the radiation cone, with phase velocity  $c_x > c_0$ , and are commonly referred to as supersonic waves. Conversely, evanescent waves are outside the radiation cone, with phase velocity  $c_x < c_0$ , and are commonly referred to as subsonic waves.

## 2.4 Encoding the dispersion relation with the Poincaré group

From a geometric perspective, we have seen in the previous sections that the dispersion relation defines the radiation cone, as shown in Fig. 2. Representing a wavefront localized in the wavenumber–frequency domain needs to respect such a geometric



structure. In other words, encoding wave propagation physics into the representation system means no transformation of the signal-acquisition method can modify the dispersion relation. This is equivalent to requiring the dispersion relation to be covariant with respect to the group of transformations underlying the signal representation. As shown in Fig. 1(c), experimental evidence suggests that acoustic fields are localized into phase velocity cones and hyperbolic scales (or wavenumber–frequency dilations). These theoretical and experimental arguments suggest that the Poincaré group<sup>1</sup> is a natural candidate, as it is often used to describe  $d$ -dimensional space–time in special relativity theory and preserves cone symmetries. Specifically, the orbits of the Lorentz subgroup form hyperbolae in the wavenumber–frequency domain, reproducing the structures observed in experimental data. Concretely, these boosts modify the phase velocity of a wavefield while preserving its scale. Conversely, the group of (isotropic) dilations modifies the scale of the wavefield while preserving the phase velocity. For these reasons, the boostlet construction is based on the semi-direct product of the Poincaré group with dilations<sup>2</sup>.

To illustrate the above intuition in a geometric fashion, let us apply various cell partitions to the 2D wavenumber-frequency domain, as shown in Fig. 3. The radiation cone is overlaid in orange. Plane waves, wavelets, and wave atoms partition the spectrum into rectangular cells of various areas [see Figs. 3(a), (b), and (c)]. Unless the spectrum has a high enough resolution, most of the coefficients nearest the cone boundary are inside and outside, which does not respect the dispersion relation. While curvelets and shearlets, shown in Fig. 3(c), can be defined with a conic partition, their decomposition scales (corona) do not follow the hyperbolae localized into phase velocity cones as shown in Fig. 1(c), in other words, the number of shears levels required to properly represent a wavefield varies with the dilation level, making shearlets ill-suited for representing wavefields. This approach might be useful if the wave field consists of time-harmonic waves in a band-limited frequency range. Another requirement for shearlets observed in previous experimental investigations [19] is that the shearlet cones<sup>3</sup> match the radiation cone—i.e., space–time should be sampled such that the sampling wavenumber and sampling frequency are scaled by the sound speed. The directional sub-band filters proposed by Pinto and Vetterli [58], shown in Fig. 3(e), consist of band-pass filtering transient plane waves within intervals of phase velocities. These filters are closest to boostlets due to the use of phase velocity cones. The boostlet partitioning is shown in Fig. 3(f), initially proposed in [60], and composed of hyperbolae localized in phase velocity cones and a concave-shaped scaling function (more details in Sec. 3.4). The main difference between boostlets and directional filters [58] lies in the localization of narrow-band frequency content within hyperbolic bands. Localizing narrow-band frequencies in an acoustic wave field allows for a flexible description of frequency-dependent absorption and scattering phenomena, e.g., different bands can have different weights.

<sup>1</sup>The Poincaré group,  $\mathbb{P}(1, d-1) = \mathbb{R}^{1, d-1} \ltimes \mathbb{O}(1, d-1)$ , is the semi-direct product of two subgroups: (i) translations  $\mathbb{R}^{1, d-1}$ , and (ii) the Lorentz group  $\mathbb{O}(1, d-1)$ , consisting of Lorentz (hyperbolic) boosts, in  $d$ -dimensional space–time.

<sup>2</sup>This is known as the Weyl group in special relativity,  $\mathbb{W}(1, d-1) = \mathbb{R}^+ \ltimes \mathbb{P}(1, d-1)$ , and it is an invariance group for photons [70]. In the face of ambiguity with the Weyl–Heisenberg group in harmonic analysis, we will use the notion of a boostlet group  $\mathbb{B}$  in this paper.

<sup>3</sup>In the jargon of cone-adapted shearlets [71], their vertical and horizontal cones correspond to the far-field and near-field acoustic cones.

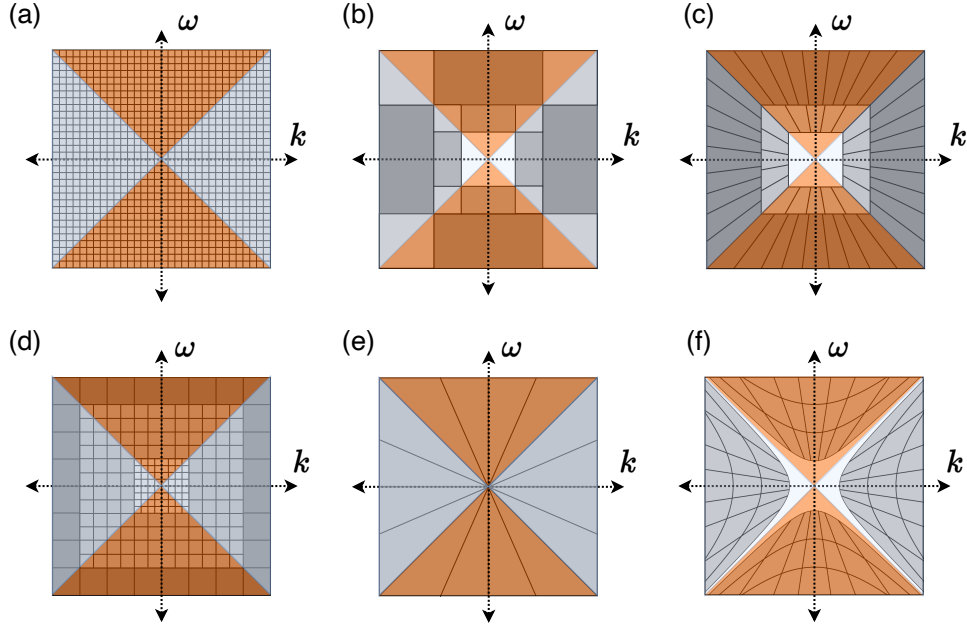


Figure 3: Tessellating the 2D wavenumber–frequency (Fourier) domain with different cell partitions. (a) Plane waves. (b) Isotropic wavelets. (c) Curvelets [42] and shearlets [43]. (d) Wave atoms [57]. (e) Directional sub-band filters [58]. (f) Boostlets. The orange cone overlaid corresponds to the radiation cone. The white regions in (b), (c), and (f) denote the wavelet, curvelet/shearlet, and boostlet scaling functions, respectively.

### 3 Continuous boostlet transform

The framework to handcraft the continuous boostlet transform, which follows the same spirit of previous harmonic analysis constructions [42, 43], is presented in this section. The derivations in this paper are in 2D space–time, that is, 1D space and time, and extensions to higher spatial dimensions are the subject of future work. The admissibility condition is derived using the group structure of the transform. Lastly, Parseval’s relationship associated with the boostlet transform is shown, leading us to the definition of the boostlet scaling function. We also visualize examples of boostlet functions, the scaling function, and their associated coefficients using an experimentally measured acoustic field.

**Definition 3.1.** Define a dilation matrix  $D_a$  and a boost matrix  $B_\theta$  acting on space–time vectors  $\zeta = (x, t)^T \in \mathbb{R}^2$  as

$$D_a = \begin{pmatrix} a & 0 \\ 0 & a \end{pmatrix}, \quad B_\theta = \begin{pmatrix} \cosh \theta & -\sinh \theta \\ -\sinh \theta & \cosh \theta \end{pmatrix},$$

with dilation parameter  $a \in \mathbb{R}^+$ , and Lorentz boost (hyperbolic rotation) parameter  $\theta \in \mathbb{R}$ . It is often convenient to combine these two transformations into a single dilation–boost matrix  $M_{a,\theta}$  given by

$$M_{a,\theta} = D_a B_\theta = B_\theta D_a = \begin{pmatrix} a \cosh \theta & -a \sinh \theta \\ -a \sinh \theta & a \cosh \theta \end{pmatrix}.$$

**Definition 3.2.** Given a translation vector in 2D space–time  $\tau = (\tau_x, \tau_t)^\top \in \mathbb{R}^2$ , a dilation factor  $a \in \mathbb{R}^+$ , and a boost parameter  $\theta \in \mathbb{R}$ , we define the boostlet function  $\psi_{a,\theta,\tau}(\varsigma) \in L^2(\mathbb{R}^2)$  as

$$\psi_{a,\theta,\tau}(\varsigma) = a^{-1}\psi(D_a^{-1}B_\theta^{-1}(\varsigma - \tau)) = a^{-1}\psi(M_{a,\theta}^{-1}(\varsigma - \tau)), \quad (6)$$

respectively, for some mother boostlet  $\psi \in L^2(\mathbb{R}^2)$ .

Let us define the Fourier transform of spatiotemporal functions  $f(\varsigma)$  as

$$\hat{f}(\xi) = \int_{\mathbb{R}^2} f(\varsigma) e^{-2\pi i \xi^\top \varsigma} d\varsigma. \quad (7)$$

Here  $\xi$  is the wavenumber–frequency vector  $\xi = (k, \omega)^\top$  representing the spectrum of the wavefield in both space and time. It is then seen that the Fourier transform of the boostlet function is given by

$$\hat{\psi}_{a,\theta,\tau} = e^{-2\pi i \tau^\top \xi} \hat{\psi}(M_{a,\theta}^\top \xi). \quad (8)$$

In the following, we will require  $\hat{\psi}(\xi)$  to be supported in the near-field cone, i.e.  $\hat{\psi}(\xi) = 0$  for  $\xi = (k, \omega)$  such that  $|k| < |\omega|$ . This near-field boostlet can then be transformed into a far-field boostlet by defining

$$\psi^*(x, t) = \psi(t, x). \quad (9)$$

This function will then have the property that  $\hat{\psi}^*(\xi) = 0$  for all  $|k| > |\omega|$ , and is thus supported in the far-field. Since the Poincaré group preserves the radiation cone, we will have that  $\psi_{a,\theta,\tau}$  and  $\psi_{a,\theta,\tau}^*$  are also supported in the near and far fields, respectively. Decomposing a wavefield  $f(x, t)$  using these boostlets gives us the desired boostlet transform.

**Definition 3.3.** Set

$$\mathbb{B} = \{(a, \theta, \tau) : a \in \mathbb{R}^+, \theta \in \mathbb{R}, \tau \in \mathbb{R}^2\}.$$

For a near-field mother boostlet  $\psi \in L^2(\mathbb{R}^2)$ , we define the *continuous boostlet transform* of a spatiotemporal function  $f(\varsigma) \in L^2(\mathbb{R}^2)$  by the mapping

$$f \rightarrow \mathcal{B}_f = (\langle f, \psi_{a,\theta,\tau} \rangle, \langle f, \psi_{a,\theta,\tau}^* \rangle)_{(a,\theta,\tau) \in \mathbb{B}}.$$

**Remark 3.1.** *The boostlet transform expands  $f$  into a redundant representation, comprised of its inner products with the boostlet functions  $\psi_{a,\theta,\tau}$  and  $\psi_{a,\theta,\tau}^*$ . From a signal-decomposition perspective, boostlets band-pass filter the signal  $f$  at various scales  $a \in \mathbb{R}^+$  (wavelength intervals) and boosts  $\theta \in \mathbb{R}$  (phase velocity intervals).*

How the set of boostlet functions respects the dispersion relation (and the acoustic radiation cone) is the subject of the following sections. In particular, while the above transform can be computed for any choice of functions  $\psi \in L^2(\mathbb{R}^2)$ , it is not clear whether the original wavefield can be recovered from the transform. To investigate this, we begin with the definition of the boostlet group, which allows us to derive an admissibility condition for  $\psi$  as well as several useful properties of the transform.

### 3.1 Boostlet group

To better understand the properties of the continuous boostlet transform defined above, we first need a more detailed characterization of the group of transformations used to generate the boostlet system.

**Lemma 3.1.** *The set  $\mathbb{B} = \mathbb{R}^+ \times \mathbb{R} \times \mathbb{R}^2$  equipped with a product  $\cdot$  given by*

$$(a, \theta, \tau) \cdot (a', \theta', \tau') = (aa', \theta + \theta', \tau + B_\theta D_a \tau')$$

*forms a group with identity  $(1, 0, 0)$ .*

*Proof.* It can be checked that  $(1, 0, 0)$  is the identity element. The inverse of an element  $(a, \theta, \tau) \in \mathbb{R}^+ \times \mathbb{R} \times \mathbb{R}^2$  is given by

$$(a, \theta, \tau)^{-1} = \left( \frac{1}{a}, -\theta, -D_a^{-1} B_\theta^{-1} \tau \right),$$

since

$$(a, \theta, \tau) \cdot \left( \frac{1}{a}, -\theta, -D_a^{-1} B_\theta^{-1} \tau \right) = \left( a \frac{1}{a}, \theta - \theta, \tau - B_\theta D_a D_a^{-1} B_\theta^{-1} \tau \right) = (1, 0, 0)$$

and

$$\left( \frac{1}{a}, -\theta, -D_a^{-1} B_\theta^{-1} \tau \right) \cdot (a, \theta, \tau) = \left( \frac{1}{a} a, -\theta + \theta, -D_a^{-1} B_\theta^{-1} \tau + B_{-\theta} D_{\frac{1}{a}} \tau \right) = (1, 0, 0).$$

The product  $\cdot$  is also associative, which is shown by

$$\begin{aligned} ((a, \theta, \tau) \cdot (a', \theta', \tau')) \cdot (a'', \theta'', \tau'') &= (aa', \theta + \theta', \tau + B_\theta D_a \tau') \cdot (a'', \theta'', \tau'') \\ &= (aa'a'', \theta + \theta' + \theta'', \tau + B_\theta D_a \tau' + B_{\theta+\theta'} D_{aa'} \tau'') \\ &= (a(a'a''), \theta + (\theta' + \theta''), \tau + B_\theta D_a (\tau' + B_{\theta'} D_{a'} \tau'')) \\ &= (a, \theta, \tau) \cdot (a'a'', \theta' + \theta'', \tau' + B_{\theta'} D_{a'} \tau'') \\ &= (a, \theta, \tau) \cdot ((a', \theta', \tau') \cdot (a'', \theta'', \tau'')), \end{aligned}$$

where we have used the fact that  $B_{\theta+\theta'} = B_\theta B_{\theta'}$  which follows from basic trigonometric identities.  $\square$

We will refer to the group  $\mathbb{B}$  with the above structure as the *boostlet group*. More generally, this can be thought of as the semi-direct product of the Poincaré group with isotropic dilations in space–time. At this point, we find no reason to dilate space–time anisotropically because the propagation medium considered in this study is non-dispersive. This can be compared to, for example, curvelets, shearlets, and related constructions, which have strong reasons to dilate real space parabolically. Incorporating such parabolic dilations in space may be sensible when extending the boostlet group to higher spatial dimensions. As it will later become evident, however, the action of the boost matrix  $B_\theta$  does generate anisotropic elements in space–time.

Let us now consider the action of the boostlet group  $\mathbb{B}$  on the space of wavefields, here represented with functions in  $L^2(\mathbb{R}^2)$ .

**Lemma 3.2.** Define  $\sigma : \mathbb{B} \rightarrow \mathfrak{U}(L^2(\mathbb{R}^2))$ , where  $\mathfrak{U}(L^2(\mathbb{R}^2))$  denotes the group of unitary operators on  $L^2(\mathbb{R}^2)$ , as

$$\sigma(a, \theta, \tau)\psi(\varsigma) = \psi_{a, \theta, \tau}(\varsigma) = a^{-1}\psi(D_a^{-1}B_\theta^{-1}(\varsigma - \tau)). \quad (10)$$

Then  $\sigma$  is a unitary representation of  $\mathbb{B}$  on  $L^2(\mathbb{R}^2)$ .

*Proof.* It can be easily checked that the action defined above satisfies the criteria for a group action on  $L^2(\mathbb{R}^2)$  and thus forms a representation of  $\mathbb{B}$ . Now let us show that this representation is unitary. Let us start by applying the inverse of  $\sigma$ , namely  $\sigma^{-1}$ , as

$$\sigma^{-1}(a, \theta, \tau)\psi(\varsigma) = a\psi(D_a B_\theta \varsigma + \tau).$$

The representation  $\sigma$  is unitary if the following relation holds for functions  $f, g \in L^2(\mathbb{R}^2)$ :

$$\langle \sigma f, g \rangle = \langle f, \sigma^* g \rangle = \langle f, \sigma^{-1} g \rangle,$$

where  $\sigma^\dagger$  is the Hermitian conjugate of  $\sigma$ . The first term is defined as

$$\langle \sigma f, g \rangle = \int a^{-1} f(B_\theta^{-1} D_a^{-1}(\varsigma - \tau)) g(\varsigma) d\varsigma,$$

while the last term is defined as

$$\langle f, \sigma^{-1} g \rangle = \int a f(\varsigma) g(D_a B_\theta \varsigma + \tau) d\varsigma.$$

Using the change of variables  $\varsigma' = D_a B_\theta \varsigma + \tau \rightarrow \varsigma = B_\theta^{-1} D_a^{-1}(\varsigma' - \tau)$ , and  $d\varsigma = |B_\theta^{-1} D_a^{-1}| d\varsigma' = a^{-2} d\varsigma'$  it follows that

$$\langle \sigma f, g \rangle = \langle f, \sigma^{-1} g \rangle = \int a^{-1} f(B_\theta^{-1} D_a^{-1}(\varsigma' - \tau)) g(\varsigma') d\varsigma'.$$

□

In addition to its group structure,  $\mathbb{B}$ , as a subset of  $\mathbb{R}^4$ , also possesses a differentiable manifold structure. Consequently,  $\mathbb{B}$  is a Lie group, which, among other things, lets us define a Haar measure on the group.

**Lemma 3.3.** The left-invariant Haar measure of  $\mathbb{B}$  is given by

$$d\mu(a, \theta, \tau) = a^{-3} da d\theta d\tau.$$

*Proof.* The left action of the boostlet group  $\mathbb{B}$  on the parameters  $(a, \theta, \tau)$  follows

$$\begin{aligned} a'' &= a' a, \\ \theta'' &= \theta' + \theta, \\ \tau'' &= \tau' + B_{\theta'} D_{a'} \tau. \end{aligned}$$

Next is to compute the determinant of the Jacobian matrix:

$$\begin{vmatrix} \frac{\partial a''}{\partial a} & \frac{\partial a''}{\partial \theta} & \frac{\partial a''}{\partial \tau_x} & \frac{\partial a''}{\partial \tau_y} \\ \frac{\partial \theta''}{\partial a} & \frac{\partial \theta''}{\partial \theta} & \frac{\partial \theta''}{\partial \tau_x} & \frac{\partial \theta''}{\partial \tau_y} \\ \frac{\partial \tau_x''}{\partial a} & \frac{\partial \tau_x''}{\partial \theta} & \frac{\partial \tau_x''}{\partial \tau_x} & \frac{\partial \tau_x''}{\partial \tau_y} \\ \frac{\partial \tau_y''}{\partial a} & \frac{\partial \tau_y''}{\partial \theta} & \frac{\partial \tau_y''}{\partial \tau_x} & \frac{\partial \tau_y''}{\partial \tau_y} \end{vmatrix} = \begin{vmatrix} a' & 0 & 0 & 0 \\ 0 & 1 & 0 & 0 \\ 0 & 0 & a' \cosh \theta' & -a' \sinh \theta' \\ 0 & 0 & -a' \sinh \theta' & a' \cosh \theta' \end{vmatrix} = a'^3.$$

□

It is known from classical wavelet theory [72] that the existence of a reproducing formula that recovers the original function from the transform relies on the admissibility of the wavelet function  $\psi$ . In light of this, we define the admissibility of the mother boostlet  $\psi$  in the following manner.

**Definition 3.4.** Let  $\psi \in L^2(\mathbb{R}^2)$  define a continuous boostlet transform  $(a, \theta, \tau) \mapsto \langle f, \psi_{a,\theta,\tau} \rangle$ . We refer to  $\psi$  as *admissible* with respect to the boostlet group  $\mathbb{B}$ , if

$$f = \int_{\mathbb{R}^2} \int_{\mathbb{B}} (\langle f, \psi_{a,\theta,\tau} \rangle \psi_{a,\theta,\tau} + \langle f, \psi_{a,\theta,\tau}^* \rangle \psi_{a,\theta,\tau}^*) \, d\mu(a, \theta, \tau) \quad (11)$$

for all  $f \in L^2(\mathbb{R}^2)$ , where  $d\mu(a, \theta, \tau)$  is the left-invariant Haar measure of  $\mathbb{B}$  (see Lemma 3.3).

A rigorous characterization of these admissible boostlets is given in Theorem 1.

### 3.2 Admissible boostlets

The next step is now to characterize the set of admissible functions  $\psi_{a,\theta,\tau} \in L^2(\mathbb{R}^2)$ . Furthermore, this section shows how the dispersion relation emerges from the admissibility condition for continuous boostlets. It is also shown that the 2D continuous boostlet transform is an isometry for  $L^2(\mathbb{R}^2)$ .

**Lemma 3.4.** Given  $f(\varsigma) \in L^2(\mathbb{R}^2)$ , a near-field boostlet function  $\psi(\varsigma) \in L^2(\mathbb{R}^2)$ , and the wavenumber–frequency vector  $\xi = (k, \omega) \in \mathbb{R}^2$ , it follows that

$$\int_{\mathbb{B}} |\langle f, \psi_{a,\theta,\tau} \rangle|^2 + |\langle f, \psi_{a,\theta,\tau}^* \rangle|^2 \frac{dad\theta d\tau}{a^3} = \int_{\mathbb{R}^2} |\hat{f}(\xi)|^2 d\xi \int_0^\infty \int_{-k'}^{k'} \frac{|\hat{\psi}(k', \omega')|^2}{k'^2 - \omega'^2} d\omega' dk'. \quad (12)$$

*Proof.* The Fourier transform of  $\psi_{a,\theta,\tau}(\varsigma)$  is

$$\hat{\psi}_{a,\theta,\tau}(\xi) = ae^{-2\pi i \tau^T \xi} \hat{\psi}(M_{a,\theta}^T \xi) \quad (13)$$

Defining  $\tilde{\psi}_{a,\theta,\tau}(\varsigma)$  as the time-reversal  $\psi_{a,\theta,\tau}(-\varsigma)$  of  $\psi_{a,\theta,\tau}(\varsigma)$ , we obtain, using Plancherel's formula, that

$$\begin{aligned} \int_{\mathbb{B}} |\langle f, \psi_{a,\theta,\tau} \rangle|^2 \frac{dad\theta d\tau}{a^3} &= \int_{\mathbb{B}} |f * \tilde{\psi}_{a,\theta,0}(\tau)|^2 \frac{dad\theta d\tau}{a^3} \\ &= \int_{\mathbb{R}^2} \int_{\mathbb{R}} \int_0^\infty |\hat{f}(\xi)|^2 \left| \widehat{\tilde{\psi}_{a,\theta,0}}(\xi) \right|^2 \frac{dad\theta}{a^3} d\xi \\ &= \int_{\mathbb{R}^2} \int_{\mathbb{R}} \int_0^\infty |\hat{f}(\xi)|^2 \left| \hat{\psi}(M_{a,\theta}^T \xi) \right|^2 \frac{dad\theta}{a} d\xi \\ &= \int_{\mathbb{R}^2} |\hat{f}(\xi)|^2 \Delta_\psi(\xi) d\xi, \end{aligned} \quad (14)$$

where

$$\begin{aligned} \Delta_\psi(\xi) &= \int_{\mathbb{R}} \int_0^\infty \left| \hat{\psi}(M_{a,\theta}^T \xi) \right|^2 \frac{dad\theta}{a} \\ &= \int_{\mathbb{R}} \int_0^\infty \left| \hat{\psi}(a(k \cosh \theta - \omega \sinh \theta), a(-k \sinh \theta + \omega \cosh \theta)) \right|^2 \frac{dad\theta}{a}. \end{aligned} \quad (15)$$

Introducing the change of variables  $k' = a(k \cosh \theta - \omega \sinh \theta)$ , and  $\omega' = a(-k \sinh \theta + \omega \cosh \theta)$ , the Jacobian gives  $dk'd\omega' = a^{-1}|k'^2 - \omega'^2|dad\theta$ . To determine the integration area, we note that  $\xi$  can be in one of the four cones defined by  $\mathcal{C}_+^{\text{near}} = \{(k, \omega) : k > 0, |\omega| < k\}$ ,  $\mathcal{C}_-^{\text{near}} = \{(k, \omega) : k < 0, |\omega| < -k\}$ ,  $\mathcal{C}_+^{\text{far}} = \{(k, \omega) : \omega > 0, |k| < \omega\}$  and  $\mathcal{C}_-^{\text{far}} = \{(k, \omega) : \omega < 0, |k| < -\omega\}$ . Let us denote this cone by  $\mathcal{C}(\xi)$ . Since the dilations and boosts preserve these cones, the variables  $(k', \omega')$  will span the entirety of the cone  $\mathcal{C}(\xi)$  to which  $\xi$  belongs. Thus, it follows that

$$\Delta_\psi(\xi) = \int_{\mathcal{C}(\xi)} \frac{|\hat{\psi}(k', \omega')|^2}{|k'^2 - \omega'^2|} dk' d\omega'. \quad (16)$$

Since we require  $\psi(\varsigma)$  to be in the near field, this integral is zero for  $\xi \in \mathcal{C}^{\text{far}} = \mathcal{C}_-^{\text{far}} \cup \mathcal{C}_+^{\text{far}}$ , while for  $\xi \in \mathcal{C}^{\text{near}} = \mathcal{C}_-^{\text{near}} \cup \mathcal{C}_+^{\text{near}}$ , it is constant. More specifically, we have

$$\Delta_\psi(\xi) = \begin{cases} 0, & \xi \in \mathcal{C}^{\text{far}}, \\ \int_{\mathcal{C}_+^{\text{near}}} \frac{|\hat{\psi}(k', \omega')|^2}{k'^2 - \omega'^2} dk' d\omega', & \xi \in \mathcal{C}^{\text{near}}, \end{cases} \quad (17)$$

where we have used the fact that  $\hat{\psi}(\xi)$  has Hermitian symmetry and therefore satisfies  $|\hat{\psi}(-\xi)|^2 = |\hat{\psi}(\xi)|^2$  so we can replace the  $\mathcal{C}_-^{\text{near}}$  with  $\mathcal{C}_+^{\text{near}}$  if necessary.

A similar argument shows that, for the far-field boostlet  $\psi^*(\varsigma)$ , we have that

$$\int_{\mathbb{B}} |\langle f, \psi_{a,\theta,\tau}^* \rangle|^2 \frac{dad\theta d\tau}{a^3} = \int_{\mathbb{R}^2} |\hat{f}(\xi)|^2 \Delta_{\psi^*}(\xi) d\xi, \quad (18)$$

where

$$\Delta_{\psi^*}(\xi) = \begin{cases} \int_{\mathcal{C}_+^{\text{far}}} \frac{|\hat{\psi}^*(k', \omega')|^2}{\omega'^2 - k'^2} dk' d\omega', & \xi \in \mathcal{C}^{\text{far}}, \\ 0, & \xi \in \mathcal{C}^{\text{near}}, \end{cases}, \quad (19)$$

which can be rewritten as

$$\Delta_{\psi^*}(\xi) = \begin{cases} \int_{\mathcal{C}_+^{\text{near}}} \frac{|\hat{\psi}(k', \omega')|^2}{k'^2 - \omega'^2} dk' d\omega', & \xi \in \mathcal{C}^{\text{far}}, \\ 0, & \xi \in \mathcal{C}^{\text{near}}, \end{cases}, \quad (20)$$

using the definition  $\psi^*(x, t) = \psi(t, x)$ .

We thus have that

$$\Delta_\psi(\xi) + \Delta_{\psi^*}(\xi) = \int_{\mathcal{C}_+^{\text{near}}} \frac{|\hat{\psi}(k', \omega')|^2}{k'^2 - \omega'^2} dk' d\omega' = \int_0^\infty \int_{-k'}^{k'} \frac{|\hat{\psi}(k', \omega')|^2}{k'^2 - \omega'^2} d\omega' dk', \quad (21)$$

for almost all  $\xi \in \mathbb{R}^2$ . □

**Theorem 1.** *Let  $\psi \in L^2(\mathbb{R}^2)$  be such that*

$$\Delta = \int_0^\infty \int_{-k}^k \frac{|\hat{\psi}(k, \omega)|^2}{k^2 - \omega^2} d\omega dk = 1. \quad (22)$$

*Then,  $\psi$  is an admissible boostlet in 2D space-time.*

*Proof.* Plugging in (22) into the identity given by Lemma 3.4, we obtain that

$$\int_{\mathbb{B}} |\langle f, \psi_{a,\theta,\tau} \rangle|^2 + |\langle f, \psi_{a,\theta,\tau}^* \rangle|^2 \frac{dad\theta d\tau}{a^3} = \int_{\mathbb{R}^2} |f(\varsigma)|^2 d\varsigma,$$

for any  $f \in L^2(\mathbb{R}^2)$ . Polarization then gives us that, for any  $f, g \in L^2(\mathbb{R}^2)$ ,

$$\int_{\mathbb{B}} \langle f, \psi_{a,\theta,\tau} \rangle \langle g, \psi_{a,\theta,\tau} \rangle + \langle f, \psi_{a,\theta,\tau}^* \rangle \langle g, \psi_{a,\theta,\tau}^* \rangle \frac{dad\theta d\tau}{a^3} = \int_{\mathbb{R}^2} f(\varsigma)g(\varsigma) d\varsigma.$$

Now, by using the adjoint of the boostlet transform, we obtain

$$\int_{\mathbb{R}^2} \int_{\mathbb{B}} \langle f, \psi_{a,\theta,\tau} \rangle \psi_{a,\theta,\tau}(\varsigma) + \langle f, \psi_{a,\theta,\tau}^* \rangle \psi_{a,\theta,\tau}^*(\varsigma) \frac{dad\theta d\tau}{a^3} g(\varsigma) d\varsigma = \int_{\mathbb{R}^2} f(\varsigma)g(\varsigma) d\varsigma.$$

Since this holds for any  $g \in L^2(\mathbb{R}^2)$ , we have that the reproducing formula

$$f(\varsigma) = \int_{\mathbb{B}} \langle f, \psi_{a,\theta,\tau} \rangle \psi_{a,\theta,\tau}(\varsigma) + \langle f, \psi_{a,\theta,\tau}^* \rangle \psi_{a,\theta,\tau}^*(\varsigma) \frac{dad\theta d\tau}{a^3}$$

holds in an  $L^2$  sense for any  $f \in L^2(\mathbb{R}^2)$ . Consequently,  $\psi$  is admissible.  $\square$

We note that the requirement that  $\Delta$  equal one in the above result can be replaced by having  $\Delta < \infty$  and dividing  $\psi$  by  $\sqrt{\Delta}$  to obtain an admissible boostlet function. Examples of admissible boostlets  $\psi \in L^2(\mathbb{R}^2)$  are tensor wavelets defined in the parameter space  $(a, \theta) \in \mathbb{R}^+ \times \mathbb{R}$  (shown in Fig. 4). To illustrate this, let us introduce a curvilinear change of coordinates for the near-field cone<sup>4</sup>. In mathematical terms, let us consider the diffeomorphism  $(k, \omega) \rightarrow (a, \theta)$  for the near-field cone such that

$$\begin{aligned} a(k, \omega) &= \sqrt{k^2 - \omega^2}, \\ \theta(k, \omega) &= \operatorname{atanh} \frac{\omega}{k}. \end{aligned} \tag{23}$$

Given the Fourier transform  $\hat{\Psi}(a, \theta)$  of analytical 2D wavelet, we can then define a boostlet through a change of variables:

$$\hat{\psi}(k, \omega) = \hat{\Psi}(a(k, \omega), \theta(k, \omega)). \tag{24}$$

Inserting this into the formula for  $\Delta$ , we obtain that

$$\Delta = \int_0^\infty \int_{\mathbb{R}} \frac{|\hat{\Psi}(a, \theta)|^2}{a} d\theta da. \tag{25}$$

In other words, we can construct  $\hat{\Psi}(a, \theta)$  as the tensor product of an admissible 1D wavelet  $\hat{\Psi}_1(a)$  and a lowpass filter  $\hat{\Psi}_2(\theta)$  and the resulting boostlet will be admissible after change of variables.

One can then define a Cartesian grid in the wavenumber–frequency domain  $(\omega, k)$ , apply the diffeomorphism (23) to said grid and sample the values of, for instance, 2D tensor Meyer wavelets in the  $(a, \theta)$  space (where we have a wavelet in the  $a$  direction and a scaling function in the  $\theta$  direction). Another example of admissible boostlets is

<sup>4</sup>It can be checked computing Christoffel symbols that Fourier space is flat.



the Mexican hat wavelet as a function of the space–time cone  $x^2 = c_0^2 t^2$ , as it will later be shown in Theorem 4.

A physical interpretation of Eq. (22) can be noted. The function emerging in the denominator,  $|\omega^2 - k^2|$ , corresponds to the Minkowski distance from the acoustic radiation cone in Fourier space, described by the dispersion relation as shown in Fig. 2. On the one hand, admissible boostlets inside the cone, i.e.,  $\omega^2 > k^2$ , are far-field waves, and admissible boostlets outside the cone, i.e.,  $\omega^2 < k^2$ , are near-field waves. On the other hand, boostlets are not admissible on the radiation cone, i.e.,  $\omega^2 = k^2$ .

**Remark 3.2.** *Admissible boostlets must be supported away from the radiation cone. Admissible far-field and near-field boostlets in non-dispersive media are separated by the radiation cone and cannot cross. This separation inevitably follows from the admissibility condition (22) and resembles the principle of causality in special relativity applied in the wavenumber–frequency domain. Note the contrast with admissible wavelets (and similarly for shearlets), which are supported away from the origin and satisfy Calderón’s condition [73]*

$$\int_{\mathbb{R} \setminus \{0\}} \frac{|\hat{\psi}(a\omega)|^2}{|\omega|} d\omega = 1, \quad \text{a.e. } \omega.$$

*The main distinction between admissible boostlets and wavelets is that wavelets are admissible provided the Euclidean norm of  $\xi$  is non-zero, while boostlets are admissible provided the norm induced by the Minkowski metric of  $\xi$  is non-zero.*

### 3.3 Visualization of admissible boostlets and expansions

This section shows examples of admissible boostlets and associated expansions with a natural acoustic field measured in 2D space–time. Examples of such functions for different wavelengths and phase velocities are shown below in Fig. 4. The convolution between these boostlet functions and an acoustic field in 2D space–time [see Figs. 4(i) and (j)] is shown in Figs. 4(k)–(n). It can be noted that, similarly to a shearlet decomposition of the acoustic field [19], boostlets extract (discard) wavefronts aligned (misaligned) with their phase velocity.

### 3.4 Scaling function

This section derives the reconstruction formula, and the scaling function associated with the boostlet transform when the sets of group parameters are bounded. In many practical applications, even in a continuous fashion, such a constraint is required [55]. It is possible to modify (11) to accommodate this instance by introducing a scaling function.

Let us consider the case in which the dilation parameter  $a$  is bounded from above by a value  $\Omega \in \mathbb{R}^+$ . As a consequence, the validity of Eq. (11) cannot be guaranteed for a generic function  $f \in L^2(\mathbb{R}^2)$  as such a requirement prevents sampling the full  $\mathbb{R}^2$  space.

**Definition 3.5.** Let the boostlet group parameters be bounded as  $a \in (0, \Omega)$  and  $\theta \in \mathbb{R}$ . Then, we can define:

$$\Delta^\Omega(\xi) = \int_0^\Omega \int_{\mathbb{R}} \left| \hat{\psi}(M_{a,\theta}^T \xi) \right|^2 + \left| \hat{\psi}^*(M_{a,\theta}^T \xi) \right|^2 \frac{dad\theta}{a} \quad (26)$$

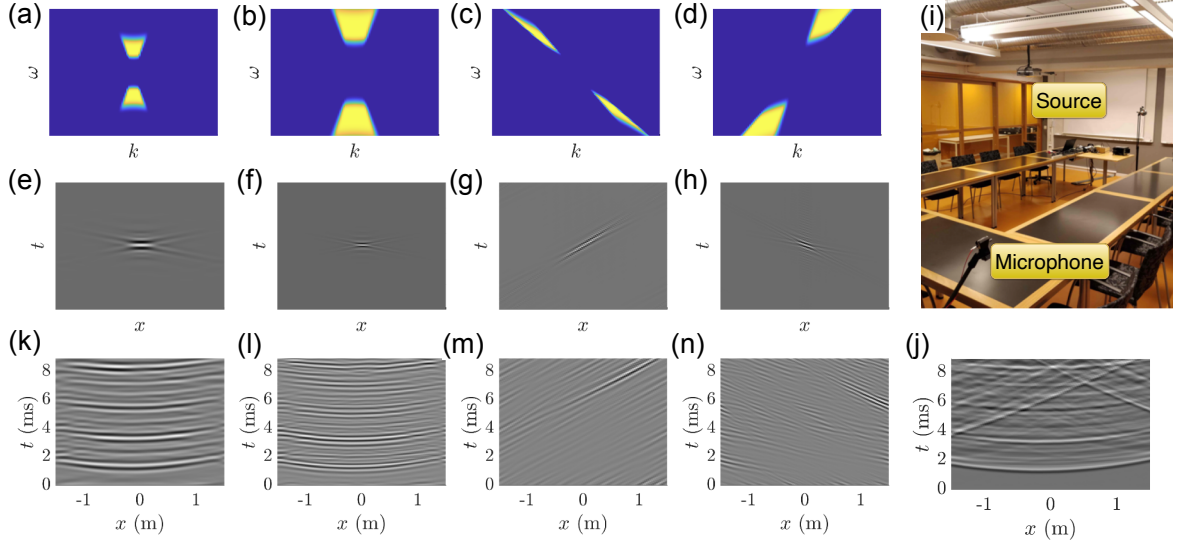


Figure 4: Prototype boostlet functions in (a)-(d) Fourier space and (e)-(h) space–time. (i) Experimental setup of room-acoustical measurement and (j) pressure field measured in space–time. (k)-(n) Convolution between the acoustic field in (j) and the boostlets in (e)-(h).

Let  $\phi(\varsigma) \in L^2(\mathbb{R}^2)$  such that

$$|\hat{\phi}(\xi)|^2 + \Delta^\Omega(\xi) = 1 \quad (27)$$

for all  $\xi \in \mathbb{R}^2$ . Then we call  $\phi(\varsigma)$  the *scaling function* associated with the boostlet  $\psi(\varsigma)$  at scale  $\Omega$ .

Denoting the translation of  $\phi(\varsigma)$

$$\phi_\tau(\varsigma) = \phi(\varsigma - \tau), \quad (28)$$

we can now form the inner products  $\langle f, \phi_\tau \rangle$  for all  $\tau \in \mathbb{R}^2$  in order to capture the parts of the signal ignored by the continuous boostlet transform when restricting it to scales below  $\Omega$ . In particular, we have the following theorem.

**Theorem 2.** *Let  $f \in L^2(\mathbb{R}^2)$ ,  $\psi \in L^2(\mathbb{R}^2)$  be an admissible boostlet, and  $\phi \in L^2(\mathbb{R}^2)$  be its associated scaling function at scale  $\Omega$ . Then, we have the following reproducing formula*

$$f(\varsigma) = \int_{\mathbb{R}^2} \langle f, \phi_\tau \rangle \phi_\tau(\varsigma) d\tau + \int_{\mathbb{R}^2} \int_{\mathbb{R}} \int_0^\Omega \langle f, \psi_{a,\theta,\tau} \rangle \psi_{a,\theta,\tau}(\varsigma) + \langle f, \psi_{a,\theta,\tau}^* \rangle \psi_{a,\theta,\tau}^*(\varsigma) \frac{dad\theta d\tau}{a^3}. \quad (29)$$

The proof is similar to that of Theorem 1.

**Remark 3.3.** *The continuous boostlet transform defined in Theorem 2 is an isometry for  $L^2(\mathbb{R}^2)$ .*

### 3.5 Visualization of boostlet scaling function and expansion

Using the diffeomorphism Eq. (23), it is possible to construct the Fourier spectrum and the space–time representation of a boostlet scaling function, shown in Figs. 5(a) and (b), respectively. The boostlet scaling function is defined in this study with a Meyer scaling function of  $a$  in the  $(a, \theta)$  space.

It can be noted that the scaling function resembles the wavenumber–frequency spectrum of a transient monopole observed in the theoretical analysis in [60]. This can be qualitatively seen with the point-like source localized in space–time in Fig. 5(b). Figure 5(c) shows the convolution between the boostlet scaling function and the acoustic field in Fig. 4(j). It can be noted that the scaling function smoothens the acoustic field. Moreover, the latter exhibits large amplitudes for waves propagating with phase velocities near the speed of sound, in correspondence with the Fourier support in Fig. 5(a).

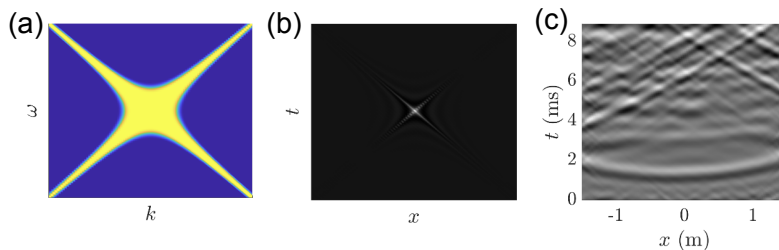


Figure 5: Prototype boostlet scaling function in (a) Fourier space and (b) space–time. (c) Convolution between the acoustic field in Fig. 4(j) and the scaling function.

Let us compare the boostlet and wavelet scaling functions (likewise for curvelets and shearlets) in terms of directional attributes. In the context of acoustic plane waves, directionality typically refers to the (Euclidean) angles between the wavefront and the receiver [cf.  $(\alpha, \beta)$  in Eq. (4)]. Similarly but differently, the phase velocity of the wave,  $c_x$ , governs its “directionality” in space–time. If one were to apply a wavelet decomposition to an acoustic field in space–time, the wavelet scaling function would contain plane waves with all phase velocities whose corresponding lines intersect with a square region of Fourier space [see Fig. 3(b)]. In contrast, boostlet scaling functions contain plane waves propagating with phase velocities in a concave region<sup>5</sup> of Fourier space [cf. Fig. 5(a)]. Following a similar reasoning, the wavelet scaling function has a low-pass shape, filtering *coarse* wave content from the acoustic field with all phase velocities. The boostlet scaling function has a combination of (i) a band-pass shape near the cone boundary, filtering *broadband* waves propagating with phase velocity equal to the speed of sound [cf. Fig. 5(c)], and (ii) a low-pass shape near the lines  $\omega = 0$  and  $k = 0$ , filtering *coarse* waves propagating with all phase velocities. A direct consequence is that the boostlet scaling function contains waves with multiple wavelengths and cannot resolve wavelength scales; that task is left to the boostlets.

<sup>5</sup>This unusual shape of a scaling function looks like an  $\ell_{p < 1}$  ball rotated by  $\pi/4$ .

## 4 Sparsity analysis with experimental data

This section presents an empirical analysis of the magnitude decay of the coefficients when applying the prototype boostlets from Sec. 3.3 and benchmark systems to acoustic fields measured in space–time. The fields have dimensions  $100 \times 100$ . The benchmark systems considered are Daubechies45 and Meyer wavelets [39], curvelets [74], wave atoms [75], and cone-adapted shearlets [76]. Defining the number of decomposition scales with  $S$ , we set  $S = 4$  for wavelets, curvelets, shearlets, and boostlets. This gives redundancy factors of 5.9632, 7, 2.5505, 13, and 29 for Daubechies45 wavelets, Meyer wavelets, curvelets, shearlets, and boostlets<sup>6</sup>, respectively. We use the default settings for wave atoms, which have a redundancy factor of 52.4288. Similar to the paper by Candès et al. [74], we compensate for the redundancy of the transforms by normalizing the 20 000 largest coefficients by their  $\ell_2$ -norm to preserve the overall signal energy. The coefficients are sorted in descending amplitude. The results are summarized in Fig. 6. The code to reproduce the results is in the GitHub repository: [https://github.com/eliaszea/ACHA\\_SparsityAnalysis](https://github.com/eliaszea/ACHA_SparsityAnalysis).

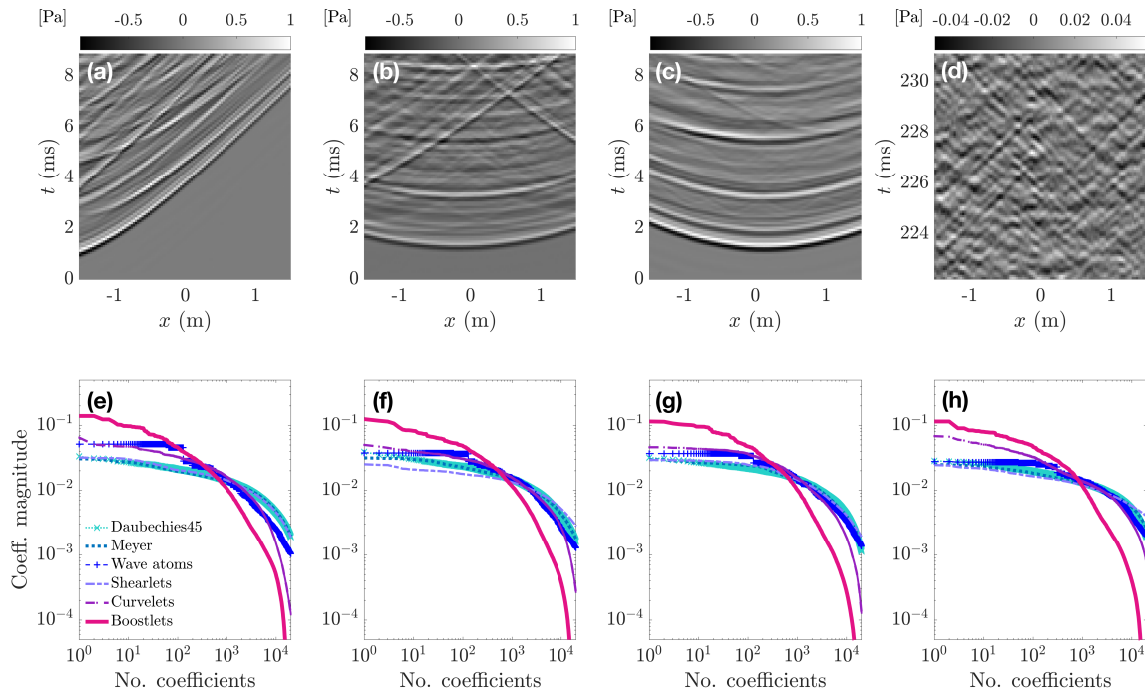


Figure 6: Sparsity analysis applying various expansions to three measured acoustic fields of space–time dimensions  $100 \times 100$ . (a)-(d): Acoustic fields in 2D space–time from experiments. (e)-(h): Magnitude of the 20 000 largest Daubechies45 wavelets, Meyer wavelets, wave atoms, curvelets, shearlets, and boostlets sorted in decreasing amplitude.

<sup>6</sup>Using the 2D tensor wavelet product in Eq. (24) and the diffeomorphism in (23), the redundancy of the boostlet transform as a function of the decomposition scales  $S$  follows:  $(S \text{ dilations}) \times (K \text{ boosts}) \times (2 \text{ cones}) + 1 \text{ scaling function}$ . Similar to the rotation and shear levels in curvelets and shearlets, the number of boost levels, here  $K = 7$ , is independent of  $S$  and can be chosen as a trade-off between tessellating Fourier space and avoiding too redundant a representation. Here, the number of boost levels is kept the same for all decomposition scales.

For the acoustic fields considered, the magnitudes of the 20 000 largest boostlet coefficients decay faster than those of the benchmarks. Wave atoms and curvelet coefficients decay similarly, with curvelets having a sharper decay above 10 000 coefficients. Shearlets, Daubechies45, and Meyer wavelets have an asymptotically similar decay. In particular, the boostlet coefficients begin to decay significantly faster than the other expansions above 1 000 coefficients.

To complement these observations, the  $\ell_1$ -norms of the 20 000 coefficients are obtained with the acoustic fields in Figs. 6(a)-(d). These norms are summarized in Table 1 below. For the acoustic fields considered, the smaller  $\ell_1$ -norm values of the

	Daubechies45	Meyer	Wave atoms	Curvelets	Shearlets	Boostlets
Fig. 6(a)	117.2	119.7	86.7	79.3	116.9	<b>45.3</b>
Fig. 6(b)	112.1	114.3	94.8	90.9	125.0	<b>47.1</b>
Fig. 6(c)	111.7	110.8	99.9	79.8	112.3	<b>41.9</b>
Fig. 6(d)	121.1	126.2	112.3	98.4	131.8	<b>46.9</b>

Table 1: The  $\ell_1$ -norms of the largest 20 000 coefficients obtained from expanding the acoustic fields in Figs. 6(a)-(d) into Daubechies45 wavelets, Meyer wavelets, wave atoms, curvelets, shearlets, and boostlets. The smallest  $\ell_1$ -norms are boldfaced.

boostlet coefficients are strong indications of sparsity. Note that the acoustic field in Fig. 6(d) is measured at a later time, having much more significant wave interference and reverberation than the fields in Figs. 6(a) and (c). For such late reverberation, the sound field becomes increasingly diffuse (i.e., waves propagate in all directions) due to the complex superposition of reflected and scattered waves from walls and objects inside the room.

It is worth stressing that the prototype boostlets used for the expansions in this section—including those shown in Fig. 4, have not been formally discretized as a frame system but with tensor Meyer wavelets using the diffeomorphism (23). Better expansions may be attainable. Although the results shown are empirical, it is promising that boostlet expansions appear to have a faster coefficient decay than the benchmark systems. A rigorous mathematical analysis of the best  $N$ -term approximation of acoustic fields, focusing on scattered waves, is the subject of future work.

## 5 Uncertainty principles and minimizers

This section presents the uncertainty principles associated with the 2D continuous boostlet transform. Uncertainty minimizers are derived for the non-commuting transform parameter pairs. We shall apply similar machinery from harmonic analysis and quantum mechanics [65, 72, 66].

**Definition 5.1.** Let  $T$  be an operator on a Hilbert space  $\mathcal{H}$  and  $\psi \in \mathcal{H}$ . The mean of the action of  $T$  on  $\psi$  is defined as

$$\mu_T(\psi) = \langle T \rangle := \int \psi^* T \psi dv$$

for some measure  $v$  in  $\mathcal{H}$ . Similarly, the variance of the action of  $T$  on  $\psi$  is defined as

$$\text{var}_T(\psi) := \langle (T - \mu_T(\psi))^2 \psi, \psi \rangle.$$

**Definition 5.2.** Let  $S$  be an operator on  $\mathcal{H}$ . The commutator  $[T, S]$  is denoted with

$$[T, S] := TS - ST.$$

The general uncertainty principle and its proof can be found in classical texts such as [77].

**Theorem 3.** *Two self-adjoint operators  $T$  and  $S$  on a Hilbert space  $\mathcal{H}$  obey the uncertainty principle*

$$\text{var}_T(\psi) \text{var}_S(\psi) \geq \frac{1}{2} |\langle [T, S] \rangle|. \quad (30)$$

*A function  $\psi$  is said to have minimal uncertainty when (30) becomes an equality. This happens if and only if there exists an  $\eta \in i\mathbb{R}$  such that*

$$(T - \mu_T(\psi))\psi = \eta(S - \mu_S(\psi))\psi. \quad (31)$$

**Theorem 4.** *(i) The infinitesimal generators of the boostlet group  $\mathbb{B}$  with respect to dilation  $a \in \mathbb{R}^+$ , boost  $\theta \in \mathbb{R}$ , and translations  $\tau = (\tau_x, \tau_t) \in \mathbb{R}^2$  are given by:*

$$\begin{aligned} (T_a\psi)(x, t) &= -i\psi - ix\frac{\partial\psi}{\partial x} - it\frac{\partial\psi}{\partial t}, \\ (T_\theta\psi)(x, t) &= it\frac{\partial\psi}{\partial x} + ix\frac{\partial\psi}{\partial t}, \\ (T_{\tau_x}\psi)(x, t) &= -i\frac{\partial\psi}{\partial x}, \\ (T_{\tau_t}\psi)(x, t) &= -i\frac{\partial\psi}{\partial t}. \end{aligned}$$

*(ii) The dilation and boost operators commute, i.e.,  $[T_a, T_\theta] = 0$ , and, unsurprisingly, so do the translation operators, i.e.,  $[T_{\tau_x}, T_{\tau_t}] = 0$ . The remaining commutators read*

$$\begin{aligned} [T_a, T_{\tau_x}] &= T_{\tau_x}, \\ [T_a, T_{\tau_t}] &= T_{\tau_t}, \\ [T_\theta, T_{\tau_x}] &= -T_{\tau_t}, \\ [T_\theta, T_{\tau_t}] &= -T_{\tau_x}, \end{aligned}$$

*which yield the following differential equations via Eq. (31):*

*(a) dilation and space-translation,*

$$-i\psi - ix\frac{\partial\psi}{\partial x} - it\frac{\partial\psi}{\partial t} - \mu_a\psi = \eta_1 \left( -i\frac{\partial\psi}{\partial x} - \mu_{\tau_x}\psi \right), \quad (32)$$

*(b) dilation and time-translation,*

$$-i\psi - ix\frac{\partial\psi}{\partial x} - it\frac{\partial\psi}{\partial t} - \mu_a\psi = \eta_2 \left( -i\frac{\partial\psi}{\partial t} - \mu_{\tau_t}\psi \right), \quad (33)$$

(c) boost and space-translation,

$$it \frac{\partial \psi}{\partial x} + ix \frac{\partial \psi}{\partial t} - \mu_\theta \psi = \eta_3 \left( -i \frac{\partial \psi}{\partial x} - \mu_{\tau_x} \psi \right), \quad (34)$$

(d) and boost and time-translation,

$$it \frac{\partial \psi}{\partial x} + ix \frac{\partial \psi}{\partial t} - \mu_\theta \psi = \eta_4 \left( -i \frac{\partial \psi}{\partial t} - \mu_{\tau_t} \psi \right). \quad (35)$$

(iii) The partial differential equations (32)-(35) do not have a simultaneous solution.  
(iv) There exists a solution for the differential equations (34) and (35), and, consequently, an uncertainty minimizer for the boost-translation pairs. This solution turns out to be the Mexican hat wavelet as a function of the space-time cone  $\rho^2 := t^2 - x^2$ :

$$\psi(x, t) = (2 - 2b\rho^2) e^{-b\rho^2}, \quad (36)$$

with  $b = -i/(2\eta)$ . It is not possible to find  $L^2(\mathbb{R}^2)$  solutions by inserting (36) into (32) and (33). However, it is possible to change the basis of the Lie algebra associated with the boostlet group and determine the uncertainty minimizer between the dilation operator  $T_a$  and the d'Alembert operator in 2D space-time (here  $c_0 = 1$  m/s):

$$\hat{T}(\psi) := \square \psi = \frac{\partial^2 \psi}{\partial x^2} - \frac{\partial^2 \psi}{\partial t^2}.$$

The minimizer is, once again, the Mexican hat wavelet in (36).

*Proof.* (i) The infinitesimal generators can be derived by differentiating the unitary representation of the boostlet group  $\sigma(\mathbb{B})$  with respect to its parameters and evaluating the result at the identity element. In mathematical terms:

$$\begin{aligned} (T_a \psi)(x, t) &:= i \frac{\partial}{\partial a} [\sigma(a, \theta, \tau)] \Big|_{a=1, \theta=0, \tau=(0,0)} = -i\psi - ix \frac{\partial \psi}{\partial x} - it \frac{\partial \psi}{\partial t}, \\ (T_\theta \psi)(x, t) &:= i \frac{\partial}{\partial \theta} [\sigma(a, \theta, \tau)] \Big|_{a=1, \theta=0, \tau=(0,0)} = it \frac{\partial \psi}{\partial x} + ix \frac{\partial \psi}{\partial t}, \\ (T_{\tau_x} \psi)(x, t) &:= i \frac{\partial}{\partial \tau_x} [\sigma(a, \theta, \tau)] \Big|_{a=1, \theta=0, \tau=(0,0)} = -i \frac{\partial \psi}{\partial x}, \\ (T_{\tau_t} \psi)(x, t) &:= i \frac{\partial}{\partial \tau_t} [\sigma(a, \theta, \tau)] \Big|_{a=1, \theta=0, \tau=(0,0)} = -i \frac{\partial \psi}{\partial t}. \end{aligned}$$

(ii) It can be checked that  $[T_a, T_\theta] = T_a T_\theta - T_\theta T_a = 0$ . Similar computations yield  $[T_{\tau_x}, T_{\tau_t}] = 0$ . Then, applying (31) to the non-commuting operator pairs yields the partial differential equations (32)-(35).

(iii) Suppose we find a function  $\psi$  that satisfies (32) and (33) simultaneously. Subtracting the two equations, one obtains

$$-i\eta_3 \frac{\partial \psi}{\partial x} + i\eta_4 \frac{\partial \psi}{\partial t} = \eta_3 \mu_{\tau_x} \psi - \eta_4 \mu_{\tau_t} \psi.$$

Taking the Fourier transform of the above equation reads

$$\hat{\psi}(\xi)(\eta_3 k - \eta_4 \omega - \eta_3 \mu_{\tau_x} + \eta_4 \mu_{\tau_t}) = 0,$$

which leads to the trivial solution  $\psi = 0$ . A similar argument follows for (34) and (35). We adopt the strategy in [65] to consider minimizers in the kernel of the infinitesimal generators.

(iv) Consider a smooth function  $\psi \in L^2(\mathbb{R}^2)$  of the form

$$\psi(x, t) = g\left(\sqrt{t^2 - x^2}\right) = g(\rho), \quad (37)$$

defined here as a function of the time-like cone  $t^2 - x^2 > 0$ . Then,

$$\frac{\partial g}{\partial x} = -\frac{x}{\rho} \frac{dg}{d\rho}, \quad \frac{\partial g}{\partial t} = \frac{t}{\rho} \frac{dg}{d\rho}, \quad (38)$$

and, consequently,

$$(T_\theta g)(\rho) = -it \frac{dg}{d\rho} \frac{x}{\rho} + ix \frac{dg}{d\rho} \frac{t}{\rho} = 0.$$

The latter means that  $\mu_\theta = 0$ , that (34) and (35) are simultaneously satisfied and that the minimizer  $g(\rho)$  is in the kernel of  $T_\theta$ . A canonical solution  $g(\rho) \in L^2(\mathbb{R}^2)$  is the Mexican hat wavelet in (36). It can also be shown that the Mexican hat is the uncertainty minimizer between the dilation operator  $T_a$  and the d'Alembert operator in 2D space-time,  $\hat{T}(\psi) = \square\psi$ . Using the expressions (38) one obtains

$$(T_a \psi)(\rho) = -ig - \rho \frac{dg}{d\rho}$$

and

$$(\hat{T}\psi)(\rho) = -\square g(\rho) = -\frac{d^2g}{d\rho^2} - \frac{1}{\rho} \frac{dg}{d\rho}.$$

Next, the differential equations (34) and (35) become

$$\frac{d^2g}{d\rho^2} + \left(\frac{1}{\rho} - \frac{i\rho}{\eta}\right) \frac{dg}{d\rho} + qg(\rho), \quad (39)$$

where  $q = [\mu_\square - (i + \mu_a)/\eta]$ .

To enforce  $L^2(\mathbb{R}^2)$  solutions we can insert

$$g(\rho) := h(\rho)e^{-b\rho^2},$$

into (39), which results in

$$\frac{d^2h}{d\rho^2} + \left[\frac{1}{\rho} - \left(4b + \frac{i}{\eta}\right)\rho\right] \frac{dh}{d\rho} + \left[\left(4b^2 + \frac{2ib}{\eta}\right)\rho^2 + (q - 4b)\right] h(\rho) = 0.$$

Following similar steps to Dahlke *et al.* [65], we can try to find polynomial solutions by setting  $b := -i/(2\eta)$ , which reduces the above differential equation to

$$\frac{d^2h}{d\rho^2} + \left(\frac{i\rho}{\eta} + \frac{1}{\rho}\right) \frac{dh}{d\rho} + \tilde{q}h(\rho) = 0, \quad (40)$$



where  $\tilde{q} = q + 2i/\eta$ . The differential equation (40) can have polynomial solutions if  $2i\eta + \tilde{q} = 0$ . Then, polynomials of the form

$$h(\rho) = h_0 + h_2\rho^2,$$

are solutions to (40) provided the coefficients  $h_0, h_2 \in \mathbb{C}$ , satisfy:

$$4h_2 + \tilde{q}h_0 = 4h_2 - \frac{2i}{\eta}h_0 = 0.$$

Lastly, the Mexican hat wavelet is recovered by setting

$$h_0 = 2, \quad h_2 = -2b = \frac{i}{\eta},$$

which gives

$$\psi(x, t) = (2 - 2b\rho^2)e^{-b\rho^2}.$$

This result is analogous for the ansatz  $\psi(x, t) = g(\rho)$  on the space-like cone, i.e.,  $\rho = \sqrt{x^2 - t^2}$ ,  $x^2 - t^2 > 0$ , by setting  $\hat{T}$  as minus the d'Alembert operator in 2D space-time,  $\hat{T}(\psi) = -\square\psi$ .  $\square$

**Remark 5.1.** *The uncertainty minimizer (36) is square-integrable and admissible. This follows immediately from the definition of the Mexican hat wavelet as a function of the space-time cone and its associated Fourier spectrum. In other words, the minimizer is supported away from the radiation cone  $\omega^2 = k^2$ .*

**Remark 5.2.** *The infinitesimal generators of the boostlet group can be interpreted as a canonical basis for the Lie algebra. The uncertainty minimizers of Theorem 4 partially preserve weak invariance with respect to a change of the basis. This remark is akin to the uncertainty minimizers of 2D wavelets [65]. For example, let us consider the nontrivial linear combinations*

$$T_1 := d_1T_\theta + d_2T_{\tau_x}, \quad S_1 := e_1T_\theta + e_2T_{\tau_t}.$$

Using a similar calculation to that in the proof of Theorem 4, it follows that

$$g''(\rho) + \left(\frac{1}{\rho} - \frac{i\rho}{\hat{\eta}}\right)g'(\rho) + \hat{q}g(\rho) = 0,$$

where

$$\hat{\eta} = \frac{\eta e_2 - d_2}{d_1 - \eta e_1},$$

$$\hat{q} = \frac{1}{\eta e_2 - d_2} [\eta e_1 \mu_a + \eta e_2 \mu_\square - d_1 \mu_a - d_2 \mu_\square - i(d_1 - \eta e_1)],$$

and, consequently,  $g(\rho) = (2 - 2\hat{b}\rho^2)e^{-\hat{b}\rho^2}$ , with  $\hat{b} = -i/(2\hat{\eta})$ .

## 6 Conclusion

This paper introduces a representation system for spatiotemporal acoustic waves that encodes the dispersion relation of the propagation medium using the Poincaré group and isotropic dilations. Several interesting results concerning admissibility conditions and uncertainty principles are discussed and interpreted physically. A sparsity analysis with experimentally measured acoustic fields shows that boostlet expansions exhibit a significantly faster coefficient decay compared to various benchmarks, including wavelets, curvelets, and wave atoms. It is noteworthy that boostlets are optimally concentrated with respect to dilation and boosting, since the infinitesimal generators of the dilation and boost operators commute, i.e.,  $\text{var}_a \text{var}_\theta \geq 0$ . This expression suggests the existence of a continuum of wave shapes where  $\text{var}_a \rightarrow 0$  or  $\infty$ , and  $\text{var}_\theta \rightarrow 0$  or  $\infty$ , which appears to include canonical wave solutions such as plane waves and spherical waves. The most straightforward case to show heuristically now is when both  $\text{var}_a \rightarrow 0$  and  $\text{var}_\theta \rightarrow 0$ , which can be recognized as a Dirac delta in wavenumber–frequency space, i.e., a stationary planar wave. Future works concern formalizing the continuum of wave shapes, deriving nonlinear approximation rates of boostlets, the operator for which they are eigenfunctions, extensions to higher spatial dimensions, and a digitally faithful implementation of the transform. In a discrete transform implementation, the isotropic dilations could be chosen such that the wavenumber–frequency bands follow hyperbolic frequency octave bands, thus having physical grounds from psychoacoustics. We deem the connections between sparse representations of acoustic fields, special relativity, quantum mechanics, and harmonic analysis fascinating. Pursuing the “momentum” of geometric multi-scale analysis [78], we hope this study stimulates encoding further physics into sparse representation systems.

## Acknowledgments

E.Z. is financially supported by the Swedish Research Council (Vetenskapsrådet) under Grant Agreement No. 2020-04668. M.L. is partly supported by the Swedish Research Council (Vetenskapsrådet) under Grant Agreement No. 2022-03032. The authors would like to thank D. Labate, F. Lizzi, U.P. Svensson, E. Fernandez-Grande, O. Öktem, and C.E. Yarman for their valuable suggestions and discussions.

## References

- [1] P. M. Morse, K. U. Ingard, *Theoretical Acoustics*, McGraw-Hill, New York, 1968. doi:10.1119/1.1976432.
- [2] A. Sommerfeld, Die greensche funktion der schwingungsgleichung., *Jahresbericht der Deutschen Mathematiker-Vereinigung* 21 (1912) 309–352. URL <http://eudml.org/doc/145344>
- [3] J. C. Allred, A. Newhouse, Applications of the Monte Carlo Method to Architectural Acoustics, *The Journal of the Acoustical Society of America* 30 (1) (1958) 1–3.

- [4] M. R. Schroeder, B. S. Atal, C. Bird, Digital computers in room acoustics, in: Proc. 4th ICA, Copenhagen M, Vol. 21, 1962, p. M21.
- [5] A. Krokstad, S. Strøm, S. Sørsdal, Calculating the acoustical room response by the use of a ray tracing technique, *Journal of Sound and Vibration* 8 (1) (1968) 118–125.
- [6] J. Allen, D. Berkley, Image method for efficiently simulating small-room acoustics, *The Journal of the Acoustical Society of America* (1979) 943–950.  
URL <http://scitation.aip.org/content/asa/journal/jasa/65/4/10.1121/1.382599>
- [7] E. G. Williams, J. D. Maynard, Holographic imaging without the wavelength resolution limit, *Phys. Rev. Lett.* 45 (1980) 554–557. doi:10.1103/PhysRevLett.45.554.  
URL <https://link.aps.org/doi/10.1103/PhysRevLett.45.554>
- [8] A. J. Berkhout, D. de Vries, J. J. Sonke, Array technology for acoustic wave field analysis in enclosures, *The Journal of the Acoustical Society of America* 102 (5) (1997) 2757–2770.
- [9] A. J. Berkhout, D. de Vries, J. Baan, B. W. van den Oetelaar, A wave field extrapolation approach to acoustical modeling in enclosed spaces, *The Journal of the Acoustical Society of America* 105 (3) (1999) 1725–1733. doi:10.1121/1.426710.
- [10] A. Craggs, A finite element method for the free vibration of air in ducts and rooms with absorbing walls, *Journal of Sound and Vibration* 173 (4) (1994) 568–576.
- [11] D. Botteldooren, Finite-difference time-domain simulation of low-frequency room acoustic problems, *The Journal of the Acoustical Society of America* 98 (6) (1995) 3302–3308. doi:10.1121/1.413817.
- [12] F. Pind, A. P. Engsig-Karup, C.-H. Jeong, J. S. Hesthaven, M. S. Mejling, J. Strømmand-Andersen, Time domain room acoustic simulations using the spectral element method, *The Journal of the Acoustical Society of America* 145 (6) (2019) 3299–3310. doi:10.1121/1.5109396.
- [13] H. Wang, I. Sihar, R. Pagán Muñoz, M. Hornikx, Room acoustics modelling in the time-domain with the nodal discontinuous Galerkin method, *The Journal of the Acoustical Society of America* 145 (4) (2019) 2650–2663. doi:10.1121/1.5096154.
- [14] E. Candès, J. Romberg, T. Tao, Robust uncertainty principles: exact signal reconstruction from highly incomplete frequency information, *IEEE Transactions on Information Theory* 52 (2) (2006) 489–509. doi:10.1109/TIT.2005.862083.
- [15] R. Mignot, L. Daudet, F. Ollivier, Room reverberation reconstruction: Interpolation of the early part using compressed sensing, *IEEE Trans. Audio, Speech Lang. Process.* 21 (11) (2013) 2301–2312. doi:10.1109/TASL.2013.2273662.

- [16] N. Antonello, E. De Sena, M. Moonen, P. A. Naylor, T. van Waterschoot, Room Impulse Response Interpolation Using a Sparse Spatio-Temporal Representation of the Sound Field, *IEEE/ACM Trans. Audio, Speech, Lang. Process.* 25 (10) (2017) 1929–1941.
- [17] S. A. Verburg, E. Fernández-Grande, Reconstruction of the sound field in a room using compressive sensing, *The Journal of the Acoustical Society of America* 143 (2018) 3770–3779. doi:10.1121/1.5042247.
- [18] F. J. Herrmann, G. Hennenfent, Non-parametric seismic data recovery with curvelet frames, *Geophysical Journal International* 173 (1) (2008) 233–248. doi:10.1111/j.1365-246X.2007.03698.x.
- [19] E. Zea, Compressed sensing of impulse responses in rooms of unknown properties and contents, *Journal of Sound and Vibration* 459 (2019) 114871. doi:https://doi.org/10.1016/j.jsv.2019.114871.
- [20] K. Shukla, P. C. Di Leoni, J. Blackshire, D. Sparkman, G. E. Karniadakis, Physics-informed neural network for ultrasound nondestructive quantification of surface breaking cracks, *Journal of Nondestructive Evaluation* 39 (3) (2020) 61.
- [21] N. Borrel-Jensen, A. P. Engsig-Karup, C.-H. Jeong, Physics-informed neural networks for one-dimensional sound field predictions with parameterized sources and impedance boundaries, *JASA Express Letters* 1 (12) (2021) 122402.
- [22] M. Rasht-Behesht, C. Huber, K. Shukla, G. E. Karniadakis, Physics-informed neural networks (pinns) for wave propagation and full waveform inversions, *Journal of Geophysical Research: Solid Earth* 127 (5) (2022) e2021JB023120. doi:https://doi.org/10.1029/2021JB023120.  
URL <https://agupubs.onlinelibrary.wiley.com/doi/abs/10.1029/2021JB023120>
- [23] L. Wang, H. Wang, L. Liang, J. Li, Z. Zeng, Y. Liu, Physics-informed neural networks for transcranial ultrasound wave propagation, *Ultrasonics* 132 (2023) 107026. doi:https://doi.org/10.1016/j.ultras.2023.107026.
- [24] X. Karakonstantis, D. Caviedes-Nozal, A. Richard, E. Fernandez-Grande, Room impulse response reconstruction with physics-informed deep learning, *The Journal of the Acoustical Society of America* 155 (2) (2024) 1048–1059.
- [25] A. Siahkoobi, G. Rizzuti, F. J. Herrmann, Weak deep priors for seismic imaging, in: *SEG Technical Program Expanded Abstracts 2020*, SEG Library, 2020, pp. 2998–3002. doi:10.1190/segam2020-3417568.1.
- [26] F. Kong, F. Picetti, V. Lipari, P. Bestagini, X. Tang, S. Tubaro, Deep prior-based unsupervised reconstruction of irregularly sampled seismic data, *IEEE Geoscience and Remote Sensing Letters* 19 (2022) 1–5. doi:10.1109/LGRS.2020.3044455.
- [27] M. Pezzoli, D. Perini, A. Bernardini, F. Borra, F. Antonacci, A. Sarti, Deep prior approach for room impulse response reconstruction, *Sensors* 22 (7) (2022).

- [28] F. Dietrichson, E. Smistad, A. Ostvik, L. Lovstakken, Ultrasound speckle reduction using generative adversarial networks, in: 2018 IEEE International Ultrasonics Symposium (IUS), 2018, pp. 1–4. doi:10.1109/ULTSYM.2018.8579764.
- [29] S. Goudarzi, A. Asif, H. Rivaz, Fast multi-focus ultrasound image recovery using generative adversarial networks, IEEE Transactions on Computational Imaging 6 (2020) 1272–1284. doi:10.1109/TCI.2020.3019137.
- [30] E. Fernandez-Grande, X. Karakonstantis, D. Caviedes-Nozal, P. Gerstoft, Generative models for sound field reconstruction, The Journal of the Acoustical Society of America 153 (2) (2023) 1179–1190.
- [31] X. Karakonstantis, E. Fernandez-Grande, Generative adversarial networks with physical sound field priors., J Acoust Soc Am 154 (2) (2023) 1226–1238.
- [32] H. Dai, M. Penwarden, R. M. Kirby, S. Joshi, Neural operator learning for ultrasound tomography inversion (2023). arXiv:2304.03297.
- [33] M. Middleton, D. T. Murphy, L. Savioja, The application of Fourier neural operator networks for solving the 2D linear acoustic wave equation, in: Proceedings of Forum Acusticum, European Acoustics Association, Turin, Italy, 2023, pp. 1–8.
- [34] H. Sun, Z. E. Ross, W. Zhu, K. Azizzadenesheli, Phase neural operator for multi-station picking of seismic arrivals, Geophysical Research Letters 50 (24) (2023) e2023GL106434. doi:https://doi.org/10.1029/2023GL106434.
- [35] N. Borrel-Jensen, S. Goswami, A. P. Engsig-Karup, G. E. Karniadakis, C.-H. Jeong, Sound propagation in realistic interactive 3D scenes with parameterized sources using deep neural operators, Proceedings of the National Academy of Sciences 121 (2) (2024) e2312159120. doi:10.1073/pnas.2312159120.
- [36] D. Gabor, Theory of communication, J. IEEE 93 (1946) 429–459.
- [37] G. Zweig, Basilar membrane motion, Cold Spring Harbor Symposia on Quantitative Biology 40 (1976) 619–633. doi:10.1101/SQB.1976.040.01.058.
- [38] A. Grossmann, J. Morlet, Decomposition of Hardy functions into square integrable wavelets of constant shape, SIAM Journal on Mathematical Analysis 15 (4) (1984) 723–736.
- [39] I. Daubechies, Ten Lectures on Wavelets, Society for Industrial and Applied Mathematics, 1992.
- [40] Y. Meyer, Wavelets and Operators, Vol. 1 of Cambridge Studies in Advanced Mathematics, Cambridge University Press, 1993. doi:10.1017/CB09780511623820.003.
- [41] E. J. Candès, D. L. Donoho, Ridgelets: A key to higher-dimensional intermittency?, Philosophical Transactions: Mathematical, Physical and Engineering Sciences 357 (1760) (1999) 2495–2509.

- [42] E. J. Candès, D. L. Donoho, New tight frames of curvelets and optimal representations of objects with piecewise C2 singularities, *Communications on Pure and Applied Mathematics* 57 (2) (2004) 219–266. doi:<https://doi.org/10.1002/cpa.10116>.
- [43] D. Labate, W.-Q. Lim, G. Kutyniok, G. Weiss, Sparse multidimensional representation using shearlets, in: M. Papadakis, A. F. Laine, M. A. Unser (Eds.), *Wavelets XI*, Vol. 5914, International Society for Optics and Photonics, SPIE, 2005, pp. 254–262. doi:<https://doi.org/10.1117/12.613494>.
- [44] M. Do, M. Vetterli, The contourlet transform: An efficient directional multiresolution image representation, *IEEE Transactions on Image Processing* 14 (12) (2005) 2091–2106. doi:[10.1109/TIP.2005.859376](https://doi.org/10.1109/TIP.2005.859376).
- [45] G. R. Easley, D. Labate, V. M. Patel, Hyperbolic shearlets, in: 2012 19th IEEE International Conference on Image Processing, 2012, pp. 2449–2452. doi:[10.1109/ICIP.2012.6467393](https://doi.org/10.1109/ICIP.2012.6467393).
- [46] P. Grohs, S. Keiper, G. Kutyniok, M. Schäfer, Alpha molecules: curvelets, shearlets, ridgelets, and beyond, in: D. V. D. Ville, V. K. Goyal, M. Papadakis (Eds.), *Wavelets and Sparsity XV*, Vol. 8858, International Society for Optics and Photonics, SPIE, 2013, p. 885804.
- [47] C. Lessig, P. Petersen, M. Schäfer, Bendlets: A second-order shearlet transform with bent elements, *Applied and Computational Harmonic Analysis* 46 (2) (2019) 384–399. doi:<https://doi.org/10.1016/j.acha.2017.06.002>.
- [48] J.-L. Starck, E. J. Candès, D. L. Donoho, The curvelet transform for image denoising, *IEEE Transactions on Image Processing* 11 (6) (2002) 670–84. doi:[10.1109/TIP.2002.1014998](https://doi.org/10.1109/TIP.2002.1014998).  
URL <http://www.ncbi.nlm.nih.gov/pubmed/18244665>
- [49] Y. Hu, J. Ren, J. Yang, R. Bai, J. Liu, Noise reduction by adaptive-sin filtering for retinal oct images, *Scientific Reports* 11 (1) (2021) 19498.
- [50] T. Gebäck, P. Koumoutsakos, Edge detection in microscopy images using curvelets, *BMC Bioinformatics* 10 (1) (2009) 75.
- [51] S. Yi, D. Labate, G. R. Easley, H. Krim, A shearlet approach to edge analysis and detection, *IEEE Transactions on Image Processing* 18 (5) (2009) 929–941. doi:[10.1109/TIP.2009.2013082](https://doi.org/10.1109/TIP.2009.2013082).
- [52] T. A. Bubba, G. Kutyniok, M. Lassas, M. März, W. Samek, S. Siltanen, V. Srinivasan, Learning the invisible: a hybrid deep learning-shearlet framework for limited angle computed tomography, *Inverse Problems* 35 (6) (2019) 064002.
- [53] M. Zhao, L. Zhu, S. Mei, Bendlets and sparse representation for biological image inpainting, in: P. You, H. Li, Z. Chen (Eds.), *Proceedings of International Conference on Image, Vision and Intelligent Systems 2022 (ICIVIS 2022)*, Springer Nature Singapore, Singapore, 2023, pp. 144–154.

- [54] E. J. Candès, D. L. Donoho, Continuous curvelet transform: I. resolution of the wavefront set, *Applied and Computational Harmonic Analysis* 19 (2) (2005) 162–197.
- [55] G. Kutyniok, D. Labate, Resolution of the wavefront set using continuous shearlets, *Transactions of the American Mathematical Society* 361 (2008) 2719–2754. doi:10.1090/s0002-9947-08-04700-4.
- [56] E. J. Candès, L. Demanet, The curvelet representation of wave propagators is optimally sparse, *Communications on Pure and Applied Mathematics* 58 (11) (2005) 1472–1528. doi:<https://doi.org/10.1002/cpa.20078>.
- [57] L. Demanet, L. Ying, Wave atoms and time upscaling of wave equations, *Numerische Mathematik* 113 (1) (2009) 1–71.
- [58] F. Pinto, M. Vetterli, Space-time-frequency processing of acoustic wave fields: Theory, algorithms, and applications, *Trans. Sig. Proc.* 58 (9) (2010) 4608–4620. doi:10.1109/TSP.2010.2052045.
- [59] C. E. Yarman, Sampling for approximating R-limited functions, *Sampling Theory in Signal and Image Processing* 19 (1) (2020) 1–48.
- [60] E. Zea, M. Laudato, On the representation of wavefronts localized in space-time and wavenumber-frequency domains, *JASA Express Letters* 1 (5) (2021) 054801. doi:10.1121/10.0004852.
- [61] T. A. Bubba, G. Easley, T. Heikkilä, D. Labate, J. P. R. Ayllon, Efficient representation of spatio-temporal data using cylindrical shearlets, *Journal of Computational and Applied Mathematics* 429 (2023) 115206. doi:<https://doi.org/10.1016/j.cam.2023.115206>.  
URL <https://www.sciencedirect.com/science/article/pii/S0377042723001504>
- [62] J. J. Bowman, T. B. A. Senior, P. L. E. Uslenghi, *Electromagnetic and Acoustic Scattering by Simple Shapes (Revised edition)*, Hemisphere Publishing, New York, 1987.
- [63] B. A. Olshausen, D. Field, Emergence of simple-cell receptive field properties by learning a sparse code for natural images, *Nature* 381 (1996) 607–609. doi:10.1038/381607a0.
- [64] D. L. Donoho, Sparse components of images and optimal atomic decompositions, *Constructive Approximation* 17 (3) (2001) 353–382.
- [65] S. Dahlke, P. Maass, The affine uncertainty principle in one and two dimensions, *Computers & Mathematics with Applications* 30 (3) (1995) 293–305.
- [66] S. Dahlke, G. Kutyniok, P. Maass, C. Sagiv, H.-G. Stark, G. Teschke, The uncertainty principle associated with the continuous shearlet transform, *International Journal of Wavelets, Multiresolution and Information Processing* 6 (2) (2008) 157–181. doi:10.1142/S021969130800229X.

- [67] E. G. Williams, *Fourier Acoustics: Sound Radiation and Nearfield Acoustical Holography*, Academic Press, London, 1999. doi:<https://doi.org/10.1016/B978-012753960-7/50001-2>.
- [68] A. Richard, E. Fernandez-Grande, J. Brunskog, C.-H. Jeong, Estimation of surface impedance at oblique incidence based on sparse array processing, *The Journal of the Acoustical Society of America* 141 (6) (2017) 4115–4125. doi:10.1121/1.4983756.  
URL <http://asa.scitation.org/doi/10.1121/1.4983756>
- [69] E. Fernandez-Grande, A. Xenaki, P. Gerstoft, A sparse equivalent source method for near-field acoustic holography, *The Journal of the Acoustical Society of America* 141 (1) (2017) 532–542. doi:10.1121/1.4974047.  
URL <http://asa.scitation.org/doi/10.1121/1.4974047>
- [70] W. Kopczyński, J. McCrea, F. W. Hehl, The Weyl group and its currents, *Physics Letters A* 128 (6) (1988) 313–317. doi:[https://doi.org/10.1016/0375-9601\(88\)90182-X](https://doi.org/10.1016/0375-9601(88)90182-X).  
URL <https://www.sciencedirect.com/science/article/pii/037596018890182X>
- [71] G. Kutyniok, D. Labate, Introduction to shearlets, in: G. Kutyniok, D. Labate (Eds.), *Shearlets: Multiscale Analysis for Multivariate Data*, Birkhäuser, Boston, 2012, pp. 1–38.
- [72] G. Weiss, E. N. Wilson, The mathematical theory of wavelets, in: J. Byrnes (Ed.), *Twentieth Century Harmonic Analysis — A Celebration*, Vol. 33 of NATO Science Series, Springer Netherlands, Dordrecht, 2001, pp. 329–366.
- [73] A. Calderón, Intermediate spaces and interpolation, the complex method, *Studia Mathematica* 24 (2) (1964) 113–190.  
URL <http://eudml.org/doc/217085>
- [74] E. Candès, L. Demanet, D. Donoho, L. Ying, Fast discrete curvelet transforms, *Multiscale Modeling & Simulation* 5 (3) (2006) 861–899. doi:10.1137/05064182X.  
URL <https://doi.org/10.1137/05064182X>
- [75] L. Demanet, L. Ying, Wave atoms and sparsity of oscillatory patterns, *Applied and Computational Harmonic Analysis* 23 (3) (2007) 368–387.
- [76] S. Häuser, G. Steidl, Fast Finite Shearlet Transform (2014). arXiv:1202.1773.
- [77] G. B. Folland, *Harmonic Analysis in Phase Space*. (AM-122), Volume 122, Princeton University Press, Princeton, 1989. doi:doi:10.1515/9781400882427.  
URL <https://doi.org/10.1515/9781400882427>
- [78] D. L. Donoho, Emerging applications of geometric multiscale analysis, in: *Proceedings of the ICM*, 2002, pp. 209–233.